

# Structure of *Escherichia coli* Flavodiiron Nitric Oxide Reductase

Célia V. Romão<sup>1</sup>, João B. Vicente<sup>1</sup>, Patrícia T. Borges<sup>1</sup>, Bruno L. Victor<sup>1</sup>, Pedro Lamosa<sup>1</sup>, Elísio Silva<sup>1</sup>, Luís Pereira<sup>1</sup>, Tiago M. Bandeiras<sup>1,2</sup>, Cláudio M. Soares<sup>1</sup>, Maria A. Carrondo<sup>1</sup>, David Turner<sup>1</sup>, Miguel Teixeira<sup>1</sup> and Carlos Frazão<sup>1</sup>

1 - Instituto de Tecnologia Química e Biológica António Xavier, ITQB NOVA, Av. da República, 2780-157 Oeiras, Portugal

2 - Instituto de Biologia Experimental e Tecnológica, Apartado 12, 2781-901 Oeiras, Portugal

Correspondence to Miguel Teixeira and Carlos Frazão: [miguel@itqb.unl.pt](mailto:miguel@itqb.unl.pt); [frazao@itqb.unl.pt](mailto:frazao@itqb.unl.pt)

<http://dx.doi.org/10.1016/j.jmb.2016.10.008>

Edited by M.F. Summers

## Abstract

Flavodiiron proteins (FDPs) are present in organisms from all domains of life and have been described so far to be involved in the detoxification of oxygen or nitric oxide (NO), acting as O<sub>2</sub> and/or NO reductases. The *Escherichia coli* FDP, named flavorubredoxin (FIRd), is the most extensively studied FDP. Biochemical and *in vivo* studies revealed that FIRd is involved in NO detoxification as part of the bacterial defense mechanisms against reactive nitrogen species. *E. coli* FIRd has a clear preference for NO as a substrate *in vitro*, exhibiting a very low reactivity toward O<sub>2</sub>. To contribute to the understanding of the structural features defining this substrate selectivity, we determined the crystallographic structure of *E. coli* FIRd, both in the isolated and reduced states. The overall tetrameric structure revealed a highly conserved flavodiiron core domain, with a metallo-β-lactamase-like domain containing a diiron center, and a flavodoxin domain with a flavin mononucleotide cofactor. The metal center in the oxidized state has a μ-hydroxo bridge coordinating the two irons, while in the reduced state, this moiety is not detected. Since only the flavodiiron domain was observed in these crystal structures, the structure of the rubredoxin domain was determined by NMR. Tunnels for the substrates were identified, and through molecular dynamics simulations, no differences for O<sub>2</sub> or NO permeation were found. The present data represent the first structure for a NO-selective FDP.

© 2016 Elsevier Ltd. All rights reserved.

## Introduction

Nitric oxide (NO) has a key role in biology, as an endogenously produced signaling molecule and a chemical weapon used by the innate immune system to target pathogenic microbes [1–4]. NO and derived reactive species react with a plethora of biological molecules, particularly metal centers in proteins/enzymes (e.g., heme and non-heme iron proteins), inhibiting key cellular processes. Not surprisingly, microorganisms have multiple systems to sense and detoxify NO and are endowed with repair mechanisms for the resulting cellular damage.

Through extensive studies on the effects of NO on *Escherichia coli*, different detoxification systems have been identified: flavohaemoglobin (Hmp) NO

denitrosylase/dioxygenase [5,6], multiheme nitrite reductase (NrfAB) [7–9], and flavodiiron-type NO reductase [flavorubredoxin (FIRd)] [10,11]. Quite recently, the *E. coli* hybrid cluster protein was also proposed to act as a high-affinity NO reductase [12]. All these enzymes provide a robust system to detoxify NO under different physiological conditions: at varying oxygen tensions, in the presence of nitrate or nitrite, and various stress conditions imposed on the bacterium.

*E. coli* FIRd was initially proposed by Gardner and coworkers to be a key NO scavenger under anaerobic conditions [10], and it was indeed demonstrated *in vitro* to be an efficient NO reductase (producing innocuous N<sub>2</sub>O) [11,13]. Multiple transcriptional studies also showed that *norV* and *hmp*,

respectively encoding FIRd and Hmp, are among the most upregulated *E. coli* genes after challenging cell cultures with NO, both under aerobic and anaerobic conditions [14–17]. Furthermore, in the context of host–pathogen interactions, FIRd contributes to *E. coli* survival (both commensal and enterohaemorrhagic strains) within macrophages [18,19]. Analysis of the genomes of over 100 species of the highly pathogenic enterohaemorrhagic *E. coli* O157:H7 strain led to the proposal that FIRd is a virulence factor [20].

FIRd, first reported in 1998 by Wasserfallen and coworkers [21], is a member of the flavodiiron protein (FDP) family (recently reviewed in Ref. [22]), and the recombinant protein has been extensively characterized [11,23–25]. FDPs are widespread in microbes, both prokaryotes and unicellular eukaryotes (particularly protozoa [26–28]), and in phototrophs, from cyanobacteria and unicellular algae to higher plants [29–32]. The structural core of this protein family, which gives it its name, has approximately 400 aa and is composed of an N-terminal metallo- $\beta$ -lactamase-like domain, which contains a diiron center with carboxylate and histidine ligands, and a C-terminal flavodoxin domain that has a non-covalently bound flavin mononucleotide (FMN) [33]. The amino acid sequences of several FDPs reveal extra C-terminal domains fused to the flavodiiron structural core, and the members of this family have been classified according to the nature (or absence) of these extra domains [34,35]. *E. coli* FIRd is a member of Class B FDPs, having a C-terminal rubredoxin (Rd)-like domain (hence the name FIRd) tethered to the FDP core by a ~20-aa-long flexible coil, with each of the Rd domains protruding out of the homotetramer surface [36]. The Rd domain is the enzyme electron entry point, transferring electrons through a kinetically stable flavin semiquinone to the diiron center, where reduction of NO takes place [23,24]. An extensive search of amino acid sequences using Blast revealed that Class B FDPs, or FIRds, are so far restricted to the Proteobacteria phylum of the gamma, delta, and beta classes. FIRds are quite conserved, having a minimal amino acid sequence identity of about 50%. The same degree of conservation is observed for the Rd domain alone, the main difference being the “linker” that connects the flavodiiron core to the Rd domain (our unpublished data).

FDPs can function as NO and/or O<sub>2</sub> reductases; whereas some members appear selective toward NO (e.g., *E. coli* FIRd [11,13]) or oxygen (e.g., protozoan [26–28] and methanogenic [37] FDPs), others have similar activities for either substrate [38–40]. The molecular determinants of substrate selectivity exhibited by different members of this protein family remain an open question. So far, no particular structural or functional feature can explain the preference for either O<sub>2</sub> or NO. Victor and coworkers [41]

addressed this issue by investigating the possible substrate channels for O<sub>2</sub> and NO in *Desulfovibrio gigas* FDP using molecular dynamics (MD) simulations and also the stability of both substrates in the diiron site pocket in different redox states. In line with the similar NO and O<sub>2</sub> reductase activities determined for *D. gigas* FDP [38], no differences between the substrates were found, highlighting the need for a crystallographic structure of a NO-selective FDP. To further contribute to the structural knowledge on FDPs, we now report the crystallographic structure of the NO-selective *E. coli* FIRd in the oxidized and reduced states.

## Results and Discussion

### FIRd structure determination and quality

The present work describes for the first time the crystal structure of *E. coli* FIRd. The crystallographic results presented are from three crystals, all of which are in the *P*622 space group. The denominated crystals A, B, and C and the structures were refined at 1.75 Å, 1.90 Å, and 2.65 Å resolutions, respectively. Crystals A and B were obtained under aerobic conditions and showed a brownish color corresponding to FIRd in the isolated state (oxidized form). Crystal C, also obtained under aerobic conditions, was subsequently submitted to chemical reduction by sodium dithionite (becoming colorless). Crystal A was measured at 1.6984-Å wavelength radiation, which allowed its iron atoms' positions to be determined. A search for anomalous scatterers only localized iron atoms from the diiron site, in addition to sulfur atoms from amino acid residues, the phosphorous atoms from FMN cofactor and phosphate (from the bacterial growth media), and chloride ions. The three FIRd crystal models share the same architecture, with an r.m.s.d. of 0.28 Å between Ca atoms. The structures showed electron density of only up to amino acid residue 400, instead of the expected 479 residues of the expressed and purified full-length *E. coli* FIRd molecule; none of the crystals displayed the C-terminal Rd domain. However, crystal B data allowed the detection of the heavier atoms from its [Fe-Cys4] center (discussed below). Mass spectrometry analyses of redissolved crystals evidenced the presence of integral FIRd in fully grown crystals, that is, including the C-terminal Rd domain (data not shown). The overall statistics of data processing, refinement procedures, and protein stereochemistry are within standard values (Table 1).

### FIRd overall structure

FDPs have been reported as dimers or tetramers in solution [26,28,39,42,43]. FIRd assembles as a

**Table 1.** Diffraction data collection and structure refinement parameters

	Crystal A (aerobic)	Crystal B (aerobic, Fe-S4)	Crystal C (reduced with dithionite)
Beamline, facility	ID29, ESRF	I04, DLS	ID23-EH2, ESRF
Detector	Pilatus 6M	ADSC Quantum 315	MarMosaic 225
Frame oscillation (°)	0.02	0.25	0.1
Total rotation range (°)	160.0	90	18.8 + 50.0
Space group	<i>P</i> 622	<i>P</i> 622	<i>P</i> 622
Wavelength (Å)	1.6984	0.972	0.873
Cell dimensions (Å)	<i>a</i> = <i>b</i> = 149.53, <i>c</i> = 94.50	<i>a</i> = <i>b</i> = 150.47, <i>c</i> = 95.36	<i>a</i> = <i>b</i> = 151.70, <i>c</i> = 96.50
Mosaic spread (°)	0.07	0.3	1.1–1.5
Resolution range (Å) <sup>a</sup>	129.50–1.75 (1.86–1.75)	59.07–1.90 (2.02–1.90)	45.34–2.65 (2.74–2.65)
No. of reflections	856,151 (41,987)	487,779 (45,342)	111,387 (6744)
No. of unique reflections	60,074 (7552)	49,670 (7402)	17,773 (1686)
Multiplicity	14.2 (5.6)	9.8(6.1)	6.3 (4.0)
Completeness (%)	95.5 (75.4)	98.6 (92.7)	91.0 (90.3)
CC(1/2)	100.0 (87.6)	99.9 (65.3)	99.4 (80.1)
Unmerged data $\langle I/\sigma(I) \rangle$	8.1	5.2	2.7
Merged data $\langle I/\sigma(I) \rangle$	28.4 (1.6)	16.5 (1.7)	5.9 (1.5)
<i>R</i> <sub>sym</sub> (%)	5.6 (83.9)	11.9 (105.3)	15.7 (48.1)
<i>R</i> <sub>meas</sub> (%)	5.8 (92.7)	12.5 (115.0)	17.1 (55.1)
<i>R</i> <sub>p.i.m.</sub> (%)	1.4 (22.2)	3.5 (26.7)	6.3 (26.0)
Wilson B (Å <sup>2</sup> )	23	24	18
No. of molecules in <i>a.u.</i>	1	1	1
Solvent in <i>a.u.</i> (vol/vol; %)	56	57	58
<i>V</i> <sub>M</sub> (Å <sup>3</sup> /Da)	2.78	2.85	2.92
<b>Refinement</b>			
<i>R</i> (%)	14.1	16.6	19.0
<i>R</i> <sub>work</sub> (%)	14.4	16.9	18.5
<i>R</i> <sub>free</sub> (%)	16.7	18.5	24.6
Bonds r.m.s.d. (Å)	0.015	0.014	0.015
Angles r.m.s.d. (°)	0.92	0.96	0.57
No. of residues	399	399	398
No. of solvent waters	423	396	128
Solvent/ligands moieties <sup>b</sup>	2 PO <sub>4</sub> <sup>3-</sup> ; 2 Cl <sup>-</sup> ; 2 GOL	2 PO <sub>4</sub> <sup>3-</sup> ; 1 GOL; 1 CAC, 1 ACY	–
Structure $\langle a.d.p. \rangle$ (Å <sup>2</sup> )	31	29	30
Main-chain $\langle a.d.p. \rangle$ (Å <sup>2</sup> )	28	25	27
Side-chain $\langle a.d.p. \rangle$ (Å <sup>2</sup> )	34	31	32
No. of TLS domains	15	11	7
No. of atoms modeled in multiple conformations	32	13	–
Ramachandran diagram distribution in favored and outlier regions (%)	97.2, 0.0	97.0, 0.0	96.0, 0.0
PDB entry	PDB 4D02	PDB 5LMC	PDB 5LLD

<sup>a</sup> Values in parentheses are for the highest-resolution shells.

<sup>b</sup> Phosphate (PO<sub>4</sub><sup>3-</sup>); chloride (Cl<sup>-</sup>); glycerol (GOL); cacodylate (CAC); acetic acid (ACY).

tetramer in solution, as found by size-exclusion chromatography [21] and small-angle X-ray scattering (SAXS) analysis [36]. The crystals contained a single monomer in the asymmetric unit (*a.u.*), but the crystallographic symmetry suggests dimeric or tetrameric architectures (Fig. 1a). These oligomeric arrangements are observed when the two perpendicular crystallographic 2-fold rotation axes are considered; one leads to the typical FDP's head-to-tail dimerization (Fig. 1b), with the occlusion of 12.3% of otherwise solvent-accessible surface (SAS) area and the formation of 14 hydrogen bonds and 18 salt bridges, while the other produces a further “dimerization” of the head-to-tail dimers with the occlusion of further 10.4% of SAS area and the additional formation of 2 × 12 hydrogen bonds and 2 × 4 salt bridges (all stereochemical details correspond to crystal A, the structure with the highest

resolution). The head-to-tail arrangements led to relatively compact and tight dimers. In contrast, their further “dimerization” into tetramers produced a hollow interior, flooded with solvent media in its tunnel-like structures at the interdimer interface (Fig. 1a).

The crystallographic structure of the *E. coli* FIRd monomer only includes its two first domains (see further details below): the N-terminal metallo-β-lactamase-like domain (up to residue 246) containing the diiron catalytic center, and the flavodoxin domain (residues 247 to 400) containing an FMN cofactor (Figs. 2 and 3). The N-terminal domain shows the αββα fold found in metallo-β-lactamase-like proteins, but it also includes four additional small β-chains (β<sub>3–6</sub>) building up a beta-hairpin vicinal to the diiron center, which, together with the head-to-tail oriented dimer partner, hinders the access of large substrates, such as lactams, to the

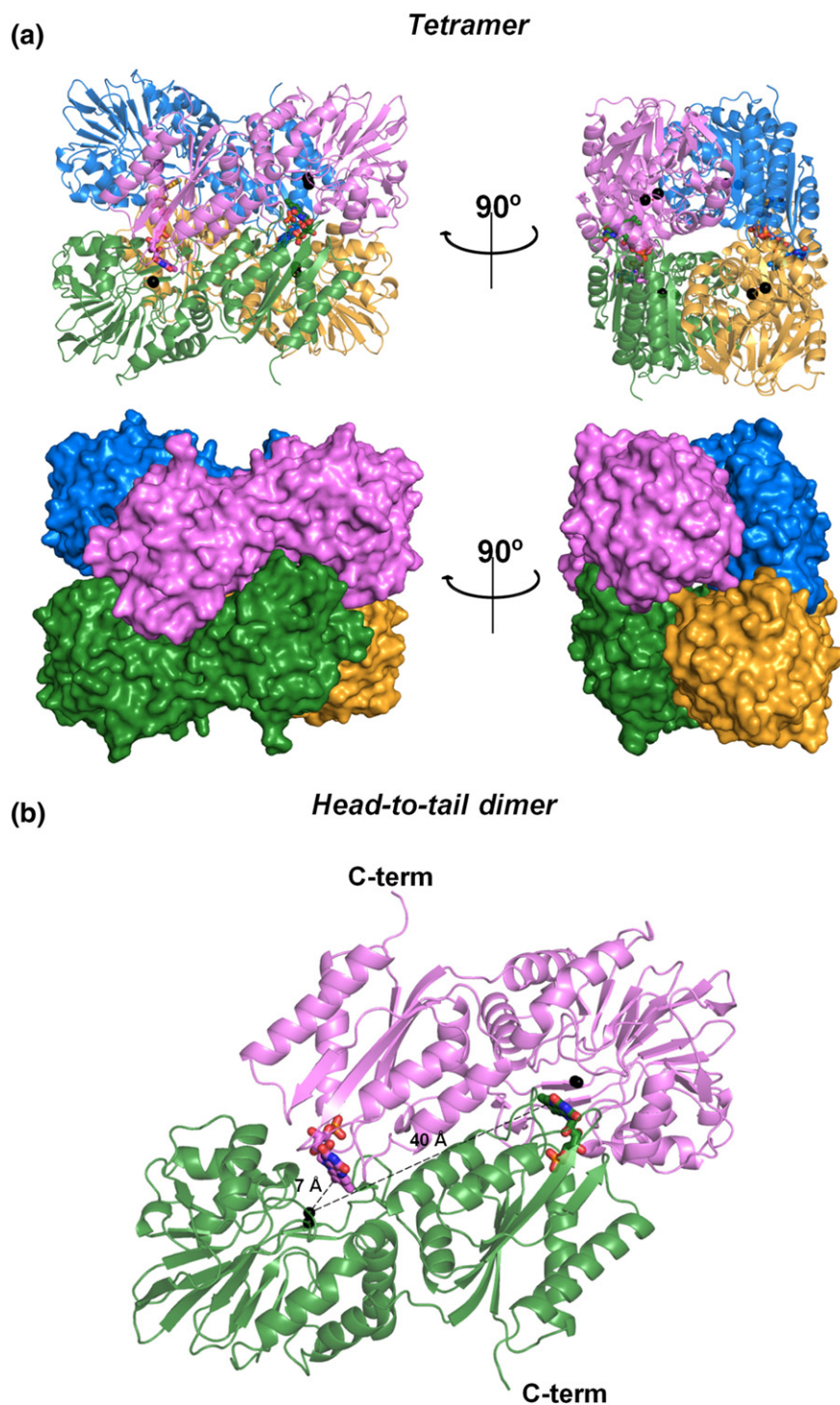


**Fig. 1.** Overall structure of *E. coli* FIRd. (a) Cartoon representation (top) and molecular surface (bottom) of the tetramer. Each monomer is represented with a different color. (b) Cartoon representation of the dimeric head-to-tail configuration. Iron atoms are represented as black spheres and FMN as sticks with carbon in green or pink, nitrogen in blue, and oxygen in red. Distances between the diiron and the FMN from the same or the head-to-tail related subunits are presented.

diiron center (Fig. 2), as observed for the other FDP structures. The flavodoxin domain, with  $\alpha\beta\alpha$  topology (Fig. 2b), is very similar to short-chain flavodoxins. Within each monomer, the distance between the catalytic diiron center and the FMN cofactor is around 40 Å (Fig. 1b), but the head-to-tail dimerization typically found in FDPs renders the diiron site of

one monomer close to the FMN of the dimer partner. In particular, the proximal iron  $\text{Fe}_p$  (relative to FMN) has a carboxylate ligand, Glu81, with the free carboxylic oxygen at 3.5 Å from atom C8M of the FMN from the dimer partner, which allows fast electron transfer between the two redox centers (Fig. 4a). The *E. coli* FIRd dimer structure is very similar to

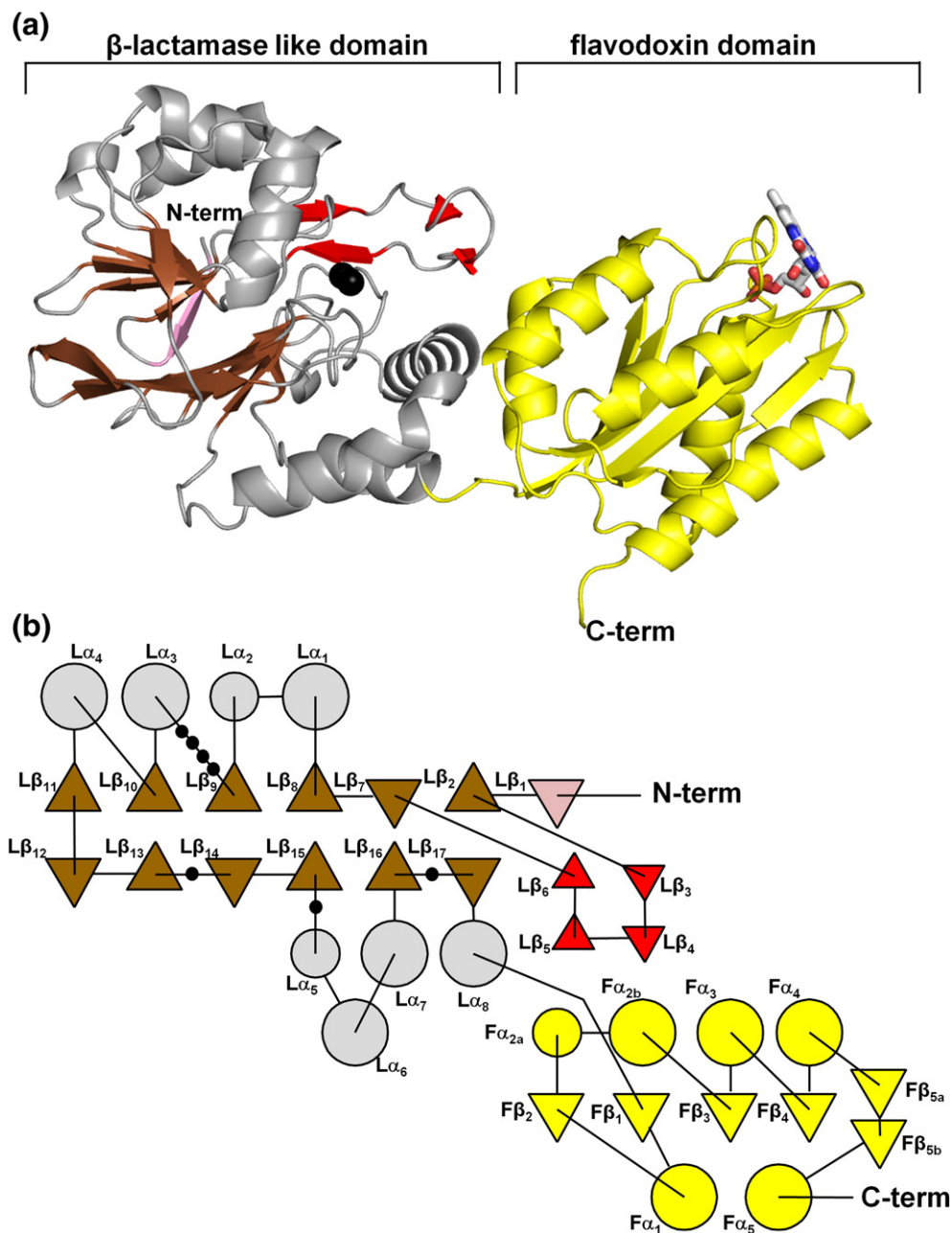


**Fig. 2.** *E. coli* FIRd monomer. (a) Cartoon representation of secondary structure elements; diiron center as black spheres and FMN as bond sticks with carbon, nitrogen, oxygen, and phosphorous atoms in white, blue, red, and orange, respectively. Conserved secondary structure elements within the  $\beta$ -lactamase-like family are colored in gray ( $\alpha$ -helices) or brown ( $\beta$ -chains). A not conserved  $\beta$ -chain is colored pink and the  $\beta$ -chains that cover the active site and are unique in FDPs are colored red. The flavodoxin domain is colored yellow. (b) Topology diagram of the monomer, with circles and triangles representing  $\alpha$ -helices and  $\beta$ -chains, respectively, color coded as in (a). Active site residues are represented as small black circles. Letters “L” and “F” are used as a prefix before the secondary structure elements, meaning those belonging to the  $\beta$ -lactamase-like and flavodoxin domains, respectively.

already available FDPs' structures (Fig. 3), their superposition leading to r.m.s.d. values within 1.2–2.3 Å for homologous C $\alpha$  positions (defined within a radius cutoff of 1.75 Å).

#### Catalytic center in FIRd

The catalytic center of FDPs, where NO or O<sub>2</sub> reduction takes place, is a non-heme diiron site

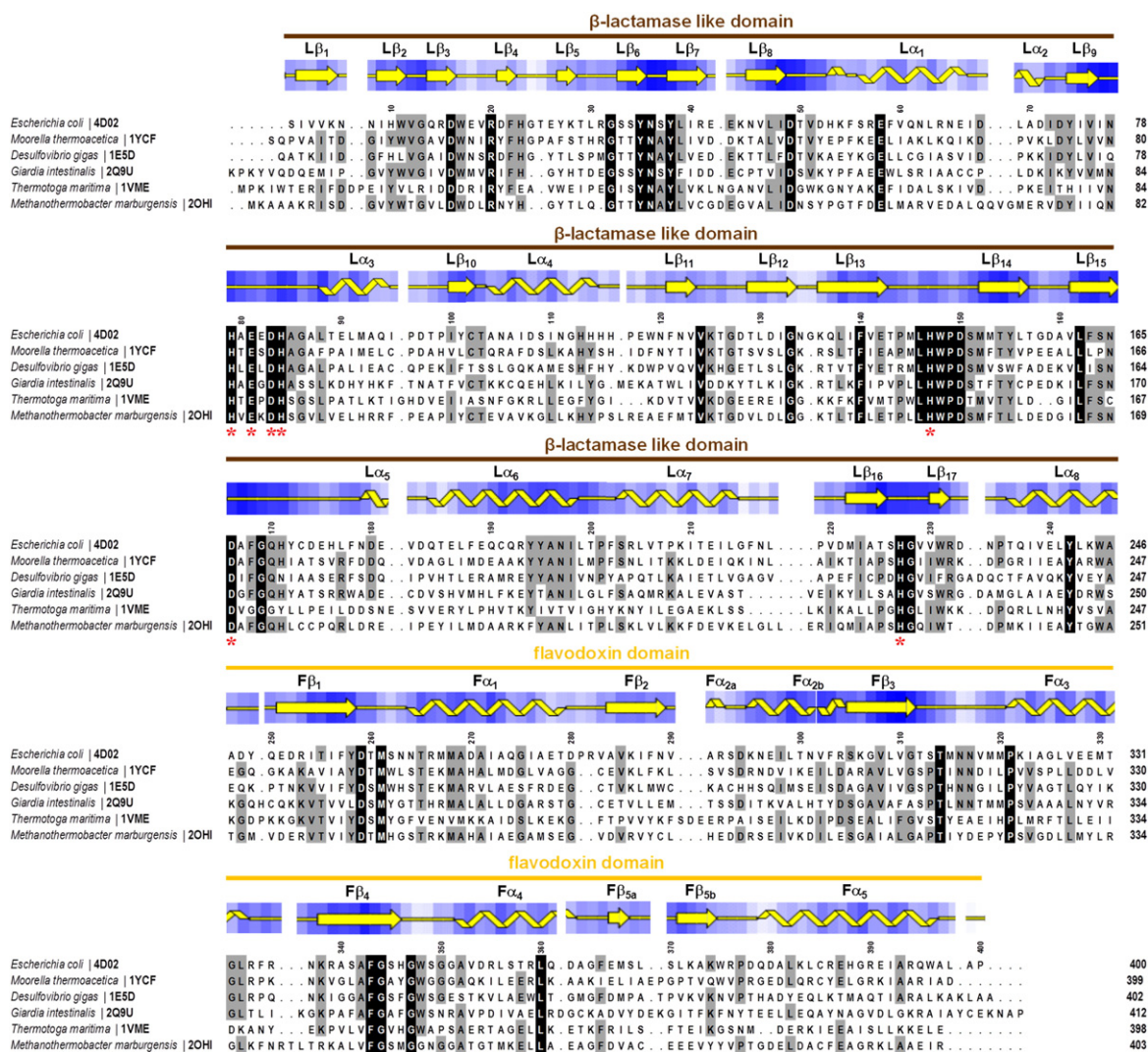


**Fig. 3.** Amino acid sequence alignment of flavodiiron proteins. Alignment based on 3D structural superpositions of *E. coli* FIRd and available FDPs structures (identified by PDB codes). *E. coli* FIRd secondary structure and amino acid residues relative solvent accessibility distribution (white to blue shading) are shown above the alignment. The different structural domains are indicated, as well as  $\alpha$ -helices and  $\beta$ -chains that are numbered according to Fig. 2b. Amino acid residues that coordinate catalytic iron atoms are indicated by \*. Strictly conserved amino acids are represented as black boxes, whereas dark gray boxes represent the mostly conserved residues among the selected sequences.

nested in the metallo- $\beta$ -lactamase-like domain. In *E. coli* FIRd, the distal iron Fe<sub>d</sub> (relative to neighboring FMN) is coordinated by the side chains of Asp83, His84, and His227, while the proximal iron Fe<sub>p</sub> is coordinated by His79, Glu81, and His147 (residues numbered according to *E. coli* FIRd, except when noted otherwise). Additionally, the Asp166 side-chain carboxylate bridges both irons (Fig. 4 and Table 2). The distances between the different ligands and iron atoms are similar among the three crystal structures (Table 2), with the exception that ligands His79 and Glu81 are closer to Fe<sub>p</sub> (distance ca 2.1 Å) in crystals A and B (oxidized forms) than in crystal C (chemically reduced form, ca 2.5 Å;

Table 2). This difference is significantly greater than the expected lengthening of a Fe–O bonding distance upon the reduction of Fe<sup>3+</sup> to Fe<sup>2+</sup>, generally within 0.03–0.06 Å [44].

In crystals A and B, the electron density showed a bridging moiety between the two iron centers unrelated to any protein residue. Its refinement as an oxygen atom led to reasonable bonding distances with both iron atoms, a hydrogen bonding distance with the free carboxylic oxygen of Fe<sub>d</sub> ligand Asp83, and consistent atomic displacement parameter (*a.d.p.*) values with its bonding partners (Fig. 4b and Table 2). As the bridging oxygen showed clear sp<sup>2</sup> configuration, it was assigned as a  $\mu$ -hydroxo



**Table 2.** Distances (Å) between irons ( $\text{Fe}_p$  and  $\text{Fe}_d$ ) and the ligating atoms from coordinating residues or other ligands.

$\text{Fe}_{\text{proximal}} - \text{Fe}_{\text{distal}}$		Crystal A	Crystal B	Crystal C
		3.5	3.5	3.2
$\text{Fe}_{\text{proximal}}$	$\text{Fe}_p$ - [His79] N <sup>E2</sup>	2.2	2.2	2.5
	$\text{Fe}_p$ - [Glu81] O <sup>E1</sup>	2.1	2.2	2.5
	$\text{Fe}_p$ - [His147] N <sup>E2</sup>	2.1	2.2	2.0
	$\text{Fe}_p$ - [Asp166] O <sup>D1</sup>	2.1	2.1	2.1
	$\text{Fe}_p$ - $\mu\text{OH}$	2.0	1.9	–
	$\text{Fe}_p$ - [PO4] O	2.3	2.7	–
	$\text{Fe}_p$ - [O <sub>2</sub> ] O1	–	–	3.4
$\text{Fe}_{\text{distal}}$	$\text{Fe}_d$ - [Asp83] O <sup>D1</sup>	2.3	2.3	2.3
	$\text{Fe}_d$ - [His84] N <sup>E2</sup>	2.1	2.0	2.0
	$\text{Fe}_d$ - [Asp166] O <sup>D1</sup>	2.1	2.1	2.2
	$\text{Fe}_d$ - [His227] N <sup>E2</sup>	2.2	2.2	2.2
	$\text{Fe}_d$ - $\mu\text{OH}$	2.1	2.0	–
	$\text{Fe}_d$ - [PO4] O	1.9	2.1	–
	$\text{Fe}_d$ - [O <sub>2</sub> ] O1	–	–	2.6

( $\mu\text{-OH}^-$ ) in order to satisfy the hydrogen bonding with the free carboxylic oxygen of Asp83. The iron ions of the two structures of the oxidized forms are therefore penta-coordinated with the side chains of the abovementioned residues and  $\mu\text{-OH}^-$ . The sixth coordination positions of both iron atoms are filled by two further oxygen atoms from a phosphate anion that occupies the active site pocket, thus producing a distorted octahedral coordination around each iron. Interestingly, neither did crystal C (chemically reduced) electron density maps show an extra electron density bridging the iron atoms nor did the refinement of a tentative  $\mu\text{-OH}^-$  produce consistent bonding distances and *a.d.p.* values (Fig. 4c). However, it is possible that this species was not detected due to the lower resolution of the structure of the reduced form. Additionally, the active site pocket in crystal C does not harbor the phosphate anion but instead an electron density blob that was fitted with a putative oxygen molecule (Fig. 4c and Table 2). Its closest oxygen atom to  $\text{Fe}_p$  or  $\text{Fe}_d$  stays at 3.4 or 2.6 Å distances, respectively, significantly longer than typical Fe–O bonding distances of about 2.1 Å [44].

At the active site, the distance between the two iron atoms diminished from 3.5 Å in the oxidized form to 3.2 Å in the reduced one. Other FDPs with structures in both redox states showed iron distance variations from 3.4 Å to 3.3 Å or 3.6 Å to 3.7 Å between the oxidized and reduced states (*Moorella thermoacetica*, PDB\_REDO codes 1YCF and 1YCG [45]; or *Methanothermobacter marburgensis*, PDB codes 2OHH and 2OHI, respectively). Thus, these data do not show a trend in FDP inter-iron distance variation with redox state, in contrast with reports on other non-heme diiron proteins with histidine and carboxylate ligands, such as ruberythrin and ribonucleotide reductase, where an increase in Fe–Fe distances by up to 0.7 Å was reported upon reduction (see Ref. [40] and references therein).

The FIRd active site pocket is lined by the above-mentioned iron ligands plus Phe22, His23, Tyr27, His171, Tyr194, and I198 (Fig. 4d and Table 4). The pocket is crossed by a tunnel that reaches the solvent media at opposite sides of the dimer (see below).

### FIRd flavin moiety

The FMN cofactor is located at the interface between each pair of head-to-tail assembled monomers and has its isoalloxazine ring at van der Waals distance from  $\text{Fe}_p$  ligand Glu81 (Fig. 4). Besides the residue Trp148, which is conserved among the FDPs presented in Fig. 3, *E. coli* FIRd also includes two further tryptophan residues, Trp348 and Trp375, with side chains vicinal to the FMN isoalloxazine ring and phosphate group, respectively (Fig. 4a). Trp348 has been proposed to modulate the visible spectral features of FDPs through a  $\pi$ -stacking interaction with the flavin isoalloxazine ring [35]. Although Trp348 and Trp375 are not conserved among all the FDPs (Fig. 3), they are strictly conserved in all FIRd sequences (data not shown). *M. marburgensis* FDP, lacking both Trp348 and Trp375, receives electrons directly from coenzyme F<sub>420</sub>, which was suggested to bind at a position equivalent to Trp348, allowing the direct interaction of the electron donor with the FMN [43].

FMN establishes contacts with several residues that interact with its phosphate group and the isoalloxazine ring. These residues can be divided into two groups: residues Thr260–Thr265 that interact mostly with the phosphate group, and residues Ser313–Asn317 and Gly347–Gly350 that interact with the isoalloxazine ring. Residue Asn316 has its main-chain amino group hydrogen bonded to the FMN isoalloxazine N5 atom and is in the same structural position as Asn315, Asn315, and Asn319 from *D. gigas*, *M. thermoacetica*, and *Giardia intestinalis* FDPs, respectively. This residue prevents FMN protonation in the semiquinone state, which indeed has an anionic character in FIRd [24] and, as also observed, in *D. gigas*, *Entamoeba histolytica*, *M. thermoacetica*, *G. intestinalis*, *Rhodobacter capsulatus*, and *Trichomonas vaginalis* FDPs [27,39,46–49].

### Rd domain in the FIRd crystal structure

In order to obtain a more complete *E. coli* FIRd structure, several crystals were produced, with their diffraction data collected and the corresponding structures refined with a protocol designed to find missing atoms or domains [50,51]. Although no crystal structure of the whole FIRd was obtained, one of the crystals (crystal B) showed in its solvent region an intriguing, well-defined tetrahedral electron density with ca 3.9-Å-long edges and roughly spherical

density blobs at its center and at each vertex (Fig. 5). This electron density was found close to residues from L $\beta$ <sub>12</sub> and L $\beta$ <sub>13</sub> of the  $\beta$ -lactamase domain, with its central spherical feature at ca 5 Å from Gln137 (Fig. 5d). As mass spectrometry analysis of the protein from redissolved crystals had assured the integrity of FIRd in the crystals, these results

suggested a disordered localization of the undetected Rd C-terminal domain, which is in accordance with previous SAXS studies of the protein in solution [36]. Although the crystal contents included species with tetrahedral geometry (cacodylate and phosphate ions), their edges' lengths only reach 2.5 or 3.0 Å, respectively, appearing as ellipsoidal electron

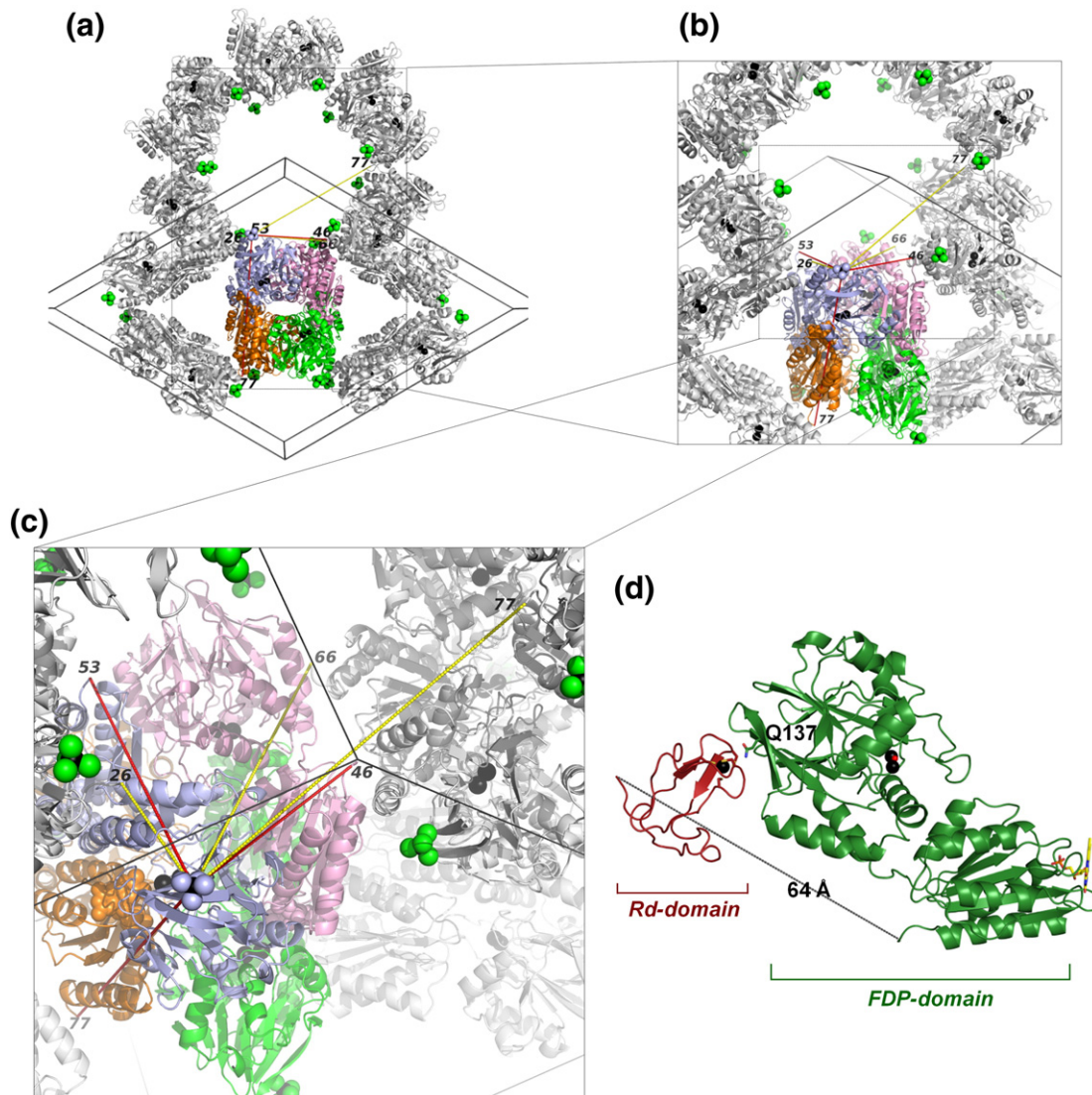


**Fig. 5.** Crystal packing of the *E. coli* FIRd and localization of Fe-4S from the Rd domain. (a) View down the 6-fold rotation axis *c*, with cell edges defining a unit cell. *E. coli* FIRd monomers represented as gray cartoons, and Fe-4S moieties as green spheres. An FIRd tetramer is highlighted using Fig. 1 colors, and the Fe-4S moiety vicinal to its blue monomer is highlighted in blue as well. The image shows that axis *c* is at the center of ca 78-Å diameter solvent channel, where Fe-4S moieties were found. The blue Fe-4S moiety was used to map the closest Pro400 C termini, either from the tetramer, mapped in red, or from other solvent channel neighbors, mapped in yellow, where the respective distances values in Å are shown. Panels (b and c) show successively zoomed-in views with other orientations of the crystal packing to help visualize the closest Pro400 C terminus to the blue Fe-4S moiety. (d) Representation of one possible orientation of Rd domain, represented in red cartoon, while the FDP domain is represented in green. The residue Gln137 from FDP domain and the cysteines that coordinate the iron from Rd domain are represented in sticks. Iron atoms are represented as black spheres, and FMN as sticks. Nitrogen and oxygen are in blue and red, while the carbons are in green for the FDP domain, red for Rd domain, and yellow for the FMN.

density shapes due to their high  $\langle a.d.p. \rangle$  values (Table 1). In contrast, the tetrahedron-shaped electron density exhibited resolved atomic densities that were initially modeled as five solvent waters. Upon refinement, the tetrahedron central water showed a significantly lower  $a.d.p.$  ( $28 \text{ \AA}^2$ ) when compared with the four adjacent vertices' waters ( $\langle a.d.p. \rangle 42 \text{ \AA}^2$ , within  $39\text{--}48 \text{ \AA}^2$ ), but such an  $a.d.p.$  distribution is not consistent with adjacent layers of waters surrounding a protein core. Additionally, as the tetrahedron edge dimensions resembled the  $S^G:S^G$  distances from a  $[\text{Fe-Cys4}]$  center of Rd, the tetrahedron density was tentatively modeled as a  $[\text{Fe-4S}^G]$  moiety. Upon refinement, the resulting  $a.d.p.$  values became closer to each other,  $57 \text{ \AA}^2$  versus  $44\text{--}58 \text{ \AA}^2$  (average  $49 \text{ \AA}^2$ ) for Fe versus  $S^G$  atoms, respectively, and all with coupled occupancy converging to 0.5. The averaged Fe– $S^G$  bond distances refined to  $2.4 \text{ \AA}$  (range  $2.2\text{--}2.5 \text{ \AA}$ ) and the  $S^G:S^G$  (tetrahedron

“edges”) dimensions refined into an average of  $3.9 \text{ \AA}$  (range  $3.6\text{--}4.0 \text{ \AA}$ ). These distances neatly compare with those of *D. gigas* Rd crystallographic structure (PDB code 2DSX [52]) determined at  $0.68\text{-\AA}$  resolution, which shows averaged Fe– $S^G$  bond distances of  $2.32 \text{ \AA}$  (range  $2.16\text{--}2.42 \text{ \AA}$ ) and averaged  $S^G:S^G$  “edges” distances of  $3.78 \text{ \AA}$  (range  $3.53\text{--}4.01 \text{ \AA}$ ). The tetrahedron density therefore seemed to display S and Fe from the “missing” Rd domain, while its lighter atoms remained not visible. This was not too surprising as these must be only partially occupied and exhibit relatively high  $a.d.p.$  values, which could be derived from the  $\sim 23\text{-aa}$ -long residue linker between the flavodoxin and Rd domains that might induce local disorder (Fig. 5).

In order to verify if the solvent region, where the putative  $[\text{Fe-4S}^G]$  moiety was found, could accommodate a Rd domain, a representative model of the *E. coli* FIRd Rd domain structure obtained by NMR

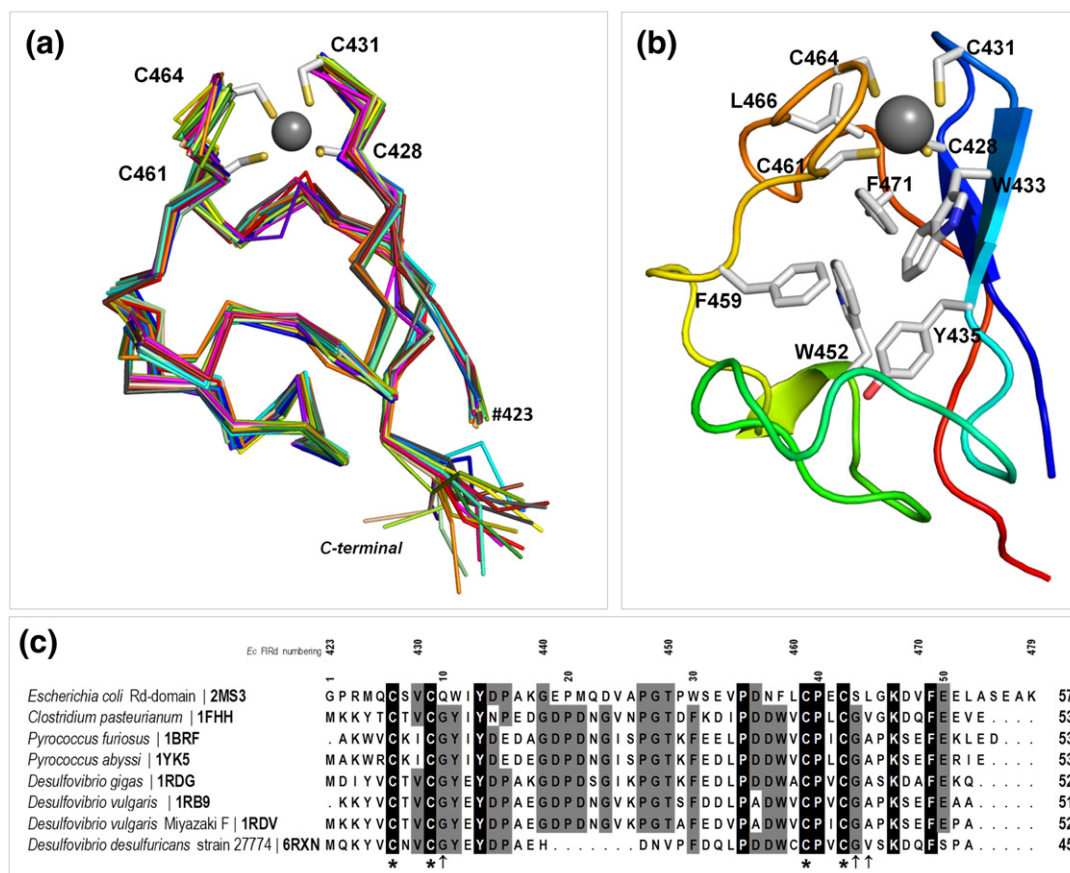


**Fig. 6.** NMR structure of *E. coli* FIRd Rd domain. (a) Polypeptide multiple structures are represented by Ca traces; the Zn atom and coordinating Cys side chains of the representative structure are represented as gray sphere and bonds sticks, respectively, color coded in white for carbon and yellow for sulfur. Amino acid residue numbering follows that of the *E. coli* FIRd full-length sequence. (b) Cartoon representation of the representative structure highlighting its secondary structure and relevant residues. (c) Amino acid sequence alignment based on Rd structures (identified by PDB codes). Strictly conserved amino acids represented as black boxes, whereas dark gray boxes represent the mostly conserved residues among the selected sequences. Cysteine ligands are indicated by \*, and those residues proposed to modulate the redox potential are indicated by †.

(see below) was tentatively positioned in the *a.u.* by fitting its [Fe–4S<sup>G</sup>] moiety into the tetrahedron-shaped electron density (Fig. 5). Among the 12 possible superposition orientations, 4 revealed minor atomic clashes against the crystal structure that would vanish upon a few rotations in dihedral angles of some Rd side chains (Fig. 5d). Such localization of the Rd domain implies overlaps with symmetry-generated Rd domains, but due to their disorder with 0.5 occupancy, such clashes are crystallographically allowed. The N termini of all four putative Rd domains (residues Gly423) were within 57–72 Å of the C terminus (residue Pro400) of their neighboring flavodiiron domain (Fig. 5d), but other symmetry-related Pro400 residues lay at closer distances (e.g., 27–32 Å) as represented in Fig. 5a–c, and it is not possible to assign definitely the visible [Fe–4S<sup>G</sup>] site to a specific symmetry operator.

Altogether, this extra density can be assigned to the loosely tethered Rd domain protruding from the FIRd flavodiiron core.

### Rd domain NMR structure

The structure of the zinc form of the *E. coli* FIRd Rd domain (truncated form consisting of residues Gly423–Lys479) was determined by NMR (Fig. 6a). The chemical shifts are deposited at BMRB with the accession number 25102. The proton signal of Ser476 NH has a weaker secondary peak separated by almost 0.1 ppm, and that of Thr450 has a distinct shoulder. Residues 477–479 gave significantly weaker signals than the rest. In the final structure calculation, 500 random conformers were minimized. There were no consistent constraint violations.

The 20 structures with the lowest target functions have been deposited in the Protein Data Bank (PDB code 2MS3); their statistics are listed in Table 3. The structures obtained are closely similar to those of single Type 1 Rds, including the chirality of the zinc coordination, although residues 477–479 are highly disordered. The pairwise r.m.s.d. in atomic coordinates were therefore calculated for residues 424–476 in the family of structures. It is likely that this disorder leads to a minor population with an alternative conformation of Ser476, giving rise to the secondary peak for the NH proton and also to the shoulder of the neighboring Thr450. No residue appears consistently in the disallowed region of the Ramachandran plot, but Gln432 and Asn458 dominate, being disallowed in 12 and 14, respectively, of the 20 structures. Both residues are in loop regions, and Gln432 is constrained by Cys431 binding to the zinc ion.

As mentioned, the overall structure determined is similar to those of single Rds, namely those from *D. gigas* (r.m.s.d. of 1.73 Å) and *Clostridium pasteurianum* (r.m.s.d. of 2.05 Å; Fig. 6b and c). Besides the conserved cysteines that are involved in iron coordination, the *E. coli* FIRd Rd domain contains

**Table 3.** NMR and refinement statistics for *E. coli* FIRd Rd domain

NMR distance constraints	
<i>Lower (and upper) volume constraints</i>	
Total NOE	859 (948)
Intraresidue	228 (235)
Sequential ( $ i - j  = 1$ )	191 (204)
Medium-range ( $ i - j  < 5$ )	141 (169)
Long-range ( $ i - j  \geq 5$ )	299 (340)
Hydrogen bonds	0
<i>Statistics for 20 structures (with r.m.s.d.)</i>	
Target function mean	3.19 (0.19)
<i>Scaling factors</i>	
Backbone protons	34.78 (0.25)
Other protons	36.87 (0.28)
Methyl to proton	48.42 (0.90)
Methyl to methyl	57.64 (0.95)
<i>Violations of upper (and lower) distance limits</i>	
Average number of violations	7 (3)
Average maximum constraint violation/Å	0.37 (0.37)
<i>Average pairwise r.m.s.d. (with r.m.s.d.)/Å</i>	
Heavy atoms	0.62 (0.11)
Backbone atoms	1.29 (0.21)
<i>Ramachandran plot (with r.m.s.d.)/%</i>	
Favored	23 (5)
Allowed	55 (7)
Generously allowed	16 (5)
Disallowed	7 (3)

other structurally relevant residues that are conserved among Rds, namely the aromatic residues Trp433, Tyr435, Trp452, Phe459, and Phe471 (Fig. 6b). Despite the overall structural similarity, the amino acid sequence identity between *E. coli* FIRd Rd domain and the other Rds presented in Fig. 6b is only ca 34%, while the sequence identity between all the others Rds is ca 61% (Fig. 6c). This suggests that the FIRd Rd domain is distantly related from the canonical Rds. Moreover, the reduction potential of the *E. coli* FIRd Rd domain is quite low as compared with those from the other Rds: –123 to –140 mV [24] compared with –50 to +30 mV for most other Rds (e.g. Refs. [53–57]); the low reduction potential of the FIRd Rd domain is important to allow favorable electron transfer to the flavin [24]. As previously proposed [25], the remarkably low reduction potential of the *E. coli* FIRd Rd center may result from a cumulative effect of substitutions in key residues amid the cysteine clusters (Fig. 6b and c). In both clusters, the substitution of the glycine typically positioned after the second cysteine by bulkier residues lowers the reduction potential in the case of *C. pasteurianum* Rd [58]. In *E. coli* FIRd, a glutamine (Gln432) and a serine (Ser465) occupy each of these positions (Fig. 6c). Moreover, after the second cysteine cluster, *E. coli* FIRd has a leucine (Leu466) in a position where the substitution of alanine by valine has been shown to result in a decrease in Rd reduction potentials [59–61].

### Substrate tunnels in FIRd

The molecular surface of *E. coli* FIRd dimer, as defined using a 1.4-Å rolling probe, evidences several tunnels and other internal pockets. The tunnel that crosses the active site pocket has two paths in opposed directions, both reaching the solvent media: a shorter path of ca 8 Å reaches the

solvent at the hollow interior of the tetramer, and a longer path of ca 19 Å extends to the tetramer external surface. The tunnel cross section varies considerably, from 2.9 to 13 Å (Fig. 7). Table 4 lists the residues that define active site pocket and tunnel paths. An analysis of the atoms lining the whole tunnel showed 67%, 64%, and 82% of apolar (carbon) atoms at the active site pocket, short and

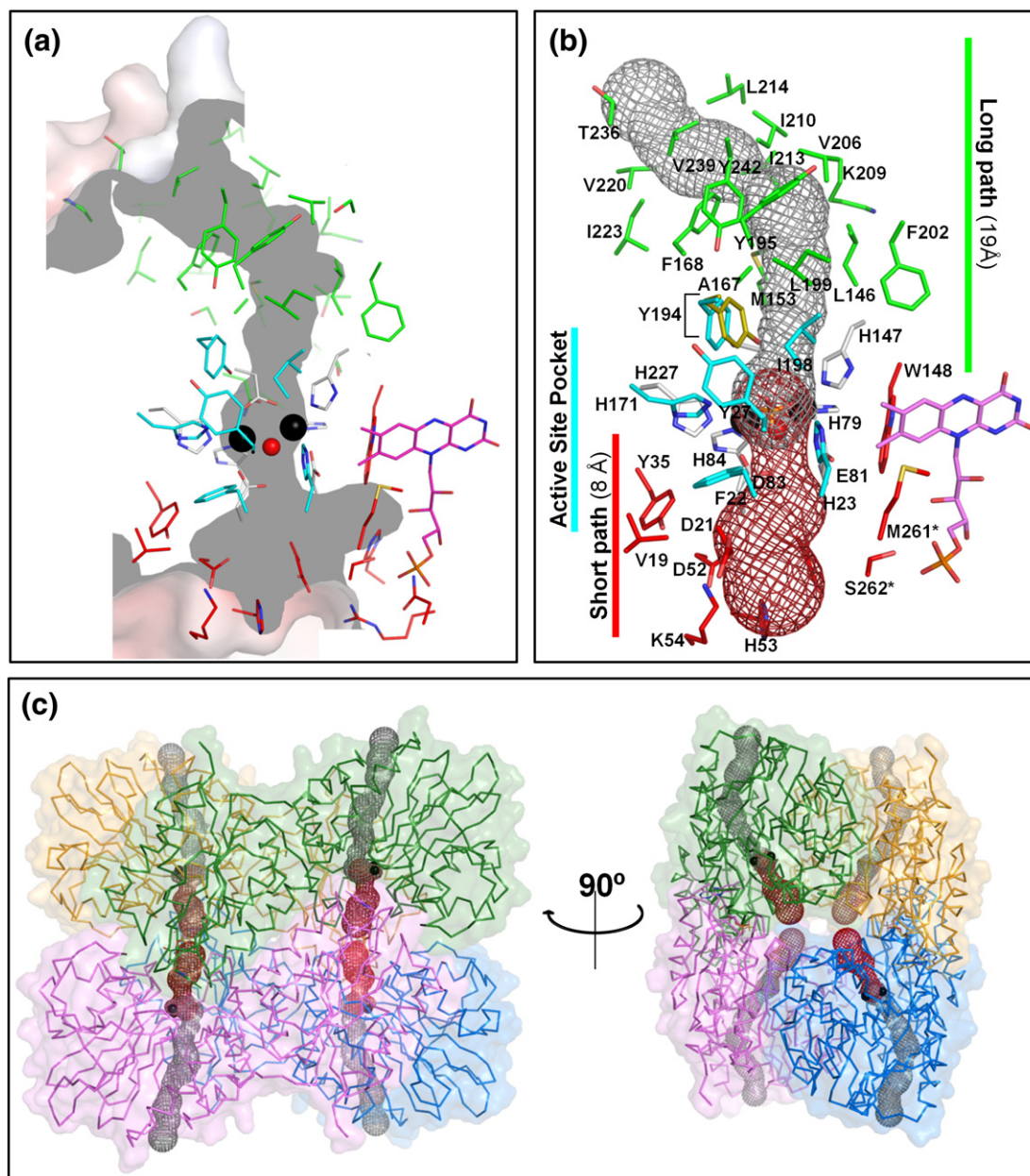


**Fig. 7.** *E. coli* FIRd tunnel. (a) Tunnel defined by a rolling sphere of 1.4 Å connects the external surface with the diiron site. (b) Its representation with MOLE highlights two sections, a long tunnel path (gray mesh) and a short tunnel path (red mesh). Amino acids lining the tunnel are represented as sticks with carbon atoms colored in green and red or cyan, for the long and short paths or the active site pocket, respectively. Tyr194 is presented both in cyan and yellow, corresponding to the conformations in crystals A and C, respectively. (c) FIRd tetramer, colored as in Fig. 1a, with transparent surface and ribbons. The tunnels are depicted as gray and red mesh.

**Table 4.** Amino acid residues that limit the different tunnels in the *E. coli* FIRd

	Residue number
Long path tunnel	Asn78,Thr126, Gly127, Ile139, Val141, Thr143, Leu146, Ser151, Met152, Met153, Thr154, Tyr155, Leu162, Ser164, Asn165, Ala167, Phe168, Tyr195, Leu199, Phe202, Ser203, Val206, Lys209, Ile210, Ile213, Leu214, Phe216, Asn217, Leu218, Val220, Ile223, Pro235, Thr236, Val239, Tyr242
Active Site Pocket	Phe22, His23, Tyr27, His171, Tyr194, Ile198 Active Site Ligands: His79, Glu81, Asp83, His84, His147, Asp166, His227
Short path tunnel	Val19, Asp21, Tyr35, Asp52, His53, Lys54, Glu82, His113, Trp148, Met261*, Ser262*, Asn264*, Arg376* and FMN*

Note: (\*) refers to residues from the head-to-tail partner.

long paths, respectively. The shorter path has an access entry of 5.5-Å diameter, includes an 8-Å-wide side gallery, and funnels down to 3.3-Å diameter at the entry of the active site pocket. The longer tunnel path has a bifurcated entry and is connected to the active site pocket through the narrowest passage of the whole tunnel. This long path starts on the external protein surface and ends at the active site pocket, where phosphate or oxygen was observed in the structures from oxidized or reduced forms, respectively. The two lower-resolution structures show here a tunnel constriction that prevents a 1.4-Å probe from crossing between the longer tunnel path and the active site pocket. This was due to a slight displacement of their Tyr194 side chain relative to its position in the highest-resolution structure (Fig. 7b). As the longer tunnel path shows higher hydrophobic character than the rest of the tunnel, it might be involved in the access of substrates to the active site. The NO or O<sub>2</sub> diffusion pathways were analyzed using MD simulations in *E. coli* FIRd (a NO-selective FDP) and in *G. intestinalis* FDP (an O<sub>2</sub>-selective enzyme) structures. In spite of the opposite substrate selectivities, both enzymes revealed similar diffusion through both paths for the two molecules (Fig. 8). The longer tunnel path is heavily populated by the diatomic molecules when compared to the shorter one (Fig. 8a). Interestingly, both tunnel paths fully match with two of the previously reported pathways, whereby O<sub>2</sub> and NO may access the diiron center of *D. gigas* FDP [41]. At the time, the authors reported the existence of three paths used both by O<sub>2</sub> and NO to access the diiron catalytic center of *D. gigas* FDP. Reported paths 1 and 3 are, respectively, equivalent to the ones reported here as the longer and shorter tunnel paths. From the MD simulations, it was also possible to observe similar amounts of NO and O<sub>2</sub> accumulating inside the tunnel and pockets of the *E. coli* and *G. intestinalis* FDPs, although the latter accumulated a slightly higher averaged number of molecules than the former (Fig. 8b). The binding affinity of O<sub>2</sub> and NO to *E. coli* and *G. intestinalis* FDPs diiron pocket was estimated using free energy calculations. Table 5 shows that the binding free energy difference between the two molecules is close to zero in both proteins, in agreement with the results reported for *D. gigas* FDP

[41]. Overall, these results suggest that the substrate selectivity observed in these proteins is related neither with the accessibility of NO versus O<sub>2</sub> to the active site nor with the relative stability of the two substrates in the active site pocket. Therefore, the observed catalytic differences might be derived from subtle differences of each enzyme, as yet to be identified.

Although the function of the long and short path channels mentioned above still needs to be established experimentally, according to the presented results and analysis of the hydrophobic environment of each path, we propose that the long path, which is more apolar, would be the entry pathway for the substrate NO/O<sub>2</sub>, whereas the exit of the more polar products, namely N<sub>2</sub>O or water, could occur through the short path. It is important to mention that in the case of the N<sub>2</sub>O product, which is a linear molecule larger than NO, the exit through the larger tunnel may be difficult due to the constrained zone, mentioned above, in which Tyr194 is involved.

### Aromatic residue chain

Recently, it has been proposed that the chains of aromatic residues, namely tryptophans and tyrosines, may function as escape routes of perilous oxidizing equivalents generated during enzymatic reactions of oxidoreductases. These routes, which use the Tyr and Trp's ability to generate delocalized radical species, connect the enzyme's active site to the protein surface, where they will be reduced by cellular reductants [62,63]. Notably, the *E. coli* FIRd crystal structure shows a chain of tyrosine and tryptophan residues, Tyr194, Tyr195, Tyr242, Trp245, and Tyr249, which "connects" the diiron site to the protein surface (Fig. 9). From those, only Tyr194 and Tyr242 are conserved among FDPs (Fig. 3). The residue Tyr249 is the one that is less conserved, which resides at the surface of the protein. The edge-to-edge distance between these residues varies within 3.7–4.8 Å. The function of these chains of aromatic residues could be to dispose the oxidizing equivalents that could be formed upon the reaction of the diiron center with oxygen, such as spurious intermediate ferryl species. It should be remembered that *E. coli* FIRd reacts with oxygen, albeit with a low affinity, and that it may also operate under aerobic

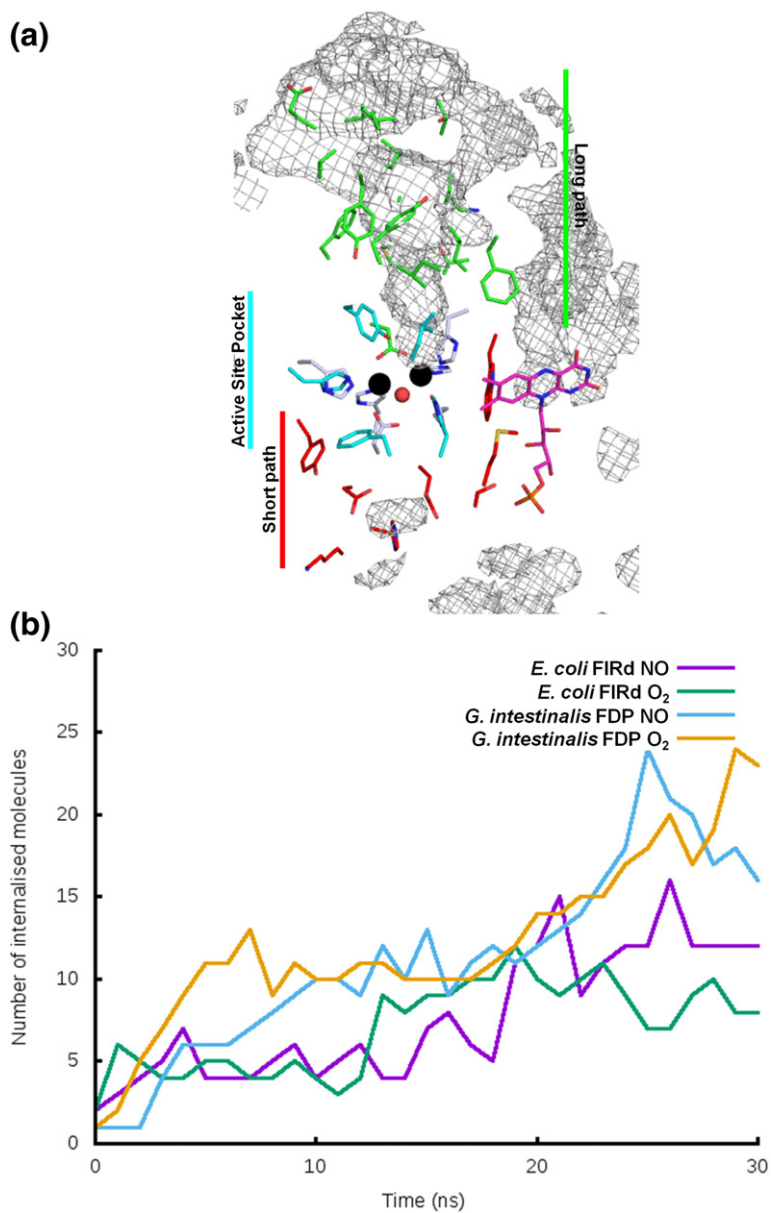


**Fig. 8.** *E. coli* FIRd and *G. intestinalis* FDP diffusion pathways for NO or O<sub>2</sub> obtained by MD simulations. (a) *E. coli* FIRd diffusion paths for O<sub>2</sub> to access the diiron catalytic region (last 10 ns of all replicates aggregated) are represented by gray density mesh. The orientation and the amino acids lining the tunnel are represented as in Fig. 7. (b) Average number of substrate molecules found inside each protein along the 30 ns of simulation.

**Table 5.** Results for the binding free energy calculations of the NO and O<sub>2</sub> simulations in the diiron site of *E. coli* FIRd and *G. intestinalis* FDP

Replicates	$\Delta G_3$ (kJ/mol)	Replicates	$\Delta G_4$ (FDP = <i>E. coli</i> FIRd) (kJ/mol)	$\Delta G_4$ (FDP = <i>G. intestinalis</i> FDP) (kJ/mol)
1	0.80	1	0.69	-0.41
2	0.77	2	-1.08	3.10
3	0.76	3	3.29	2.34
average $\pm$ std. error	$0.78 \pm 0.01$	4	3.92	-2.55
		5	-4.98	-0.55
		6	0.60	1.03
		average $\pm$ std. error	$0.41 \pm 1.33$	$0.49 \pm 0.85$
		$\Delta \Delta G = \Delta G_4 - \Delta G_3$	$-0.37 \pm 1.33$	$-0.28 \pm 0.86$

The free energy terms are the ones described on Fig. 8.

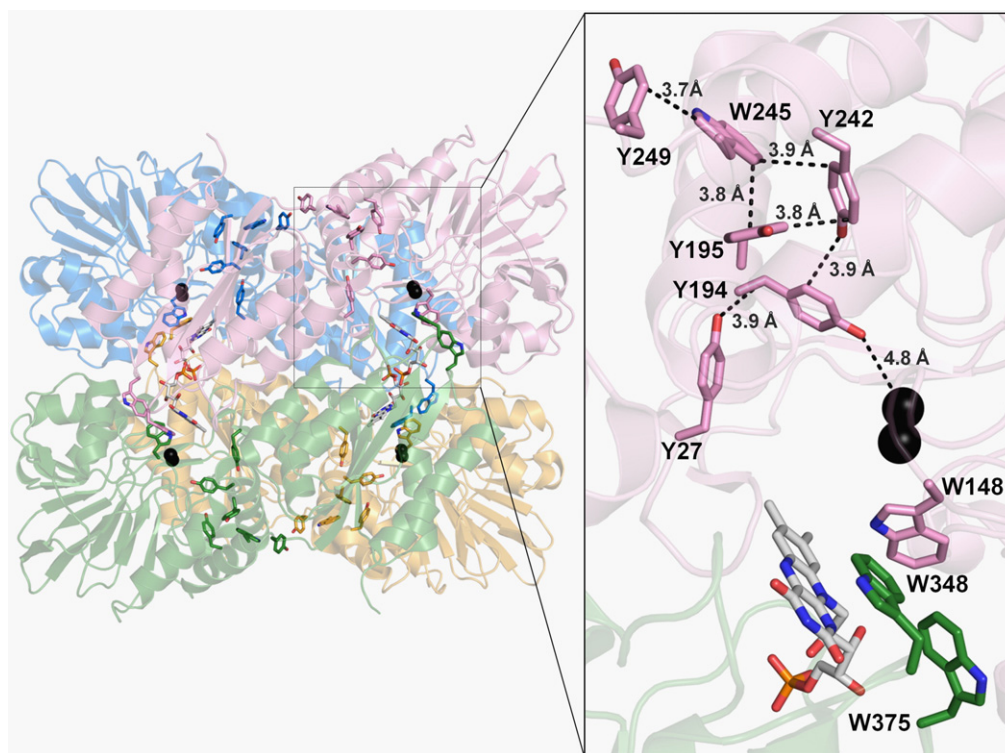


**Fig. 9.** *E. coli* FIRd chain of aromatic residues. Cartoon representation of the tetramer, with subunits colored as in Fig. 1. Zoomed-in view of the aromatic residues chain with the shortest edge-to-edge distances between residues. The tyrosine/tryptophan chain is represented as sticks. Carbons are colored according to each subunit; nitrogen in blue and oxygen in red. The iron atoms are represented as black spheres, and FMN as bonds sticks color coded as in Fig. 1.

or microaerobic conditions in NO detoxification. Those aromatic chains will most probably be even more important for the oxygen-reducing FDPs, where they are mostly conserved.

### Concluding remarks

FDPs have emerged as a detoxification system against NO and/or oxygen, affording protection from NO and oxygen in prokaryotes, anaerobic protozoa, and phototrophs. Despite several molecular and physiological studies on the members of this protein family, an open issue concerns the determinants that dictate the preference for either NO or O<sub>2</sub>. Previous studies on an oxygen-selective FDP have shown the relevance of residues in the vicinity of the diiron active site in the modulation of O<sub>2</sub> reactivity [47].

Herein, we reported the crystallographic structure of a NO-selective FDP, *E. coli* FIRd. Diffraction data were obtained for the isolated oxidized form and upon chemical reduction. The major differences between the two forms consisted of the loss of a  $\mu$ -OH<sup>-</sup> moiety bridging the two irons in the catalytic center upon reduction and the possible trapping of a reaction intermediate in the “reduced” diiron center.

FIRd also has the particular feature of being the first FDP with an extra functional domain to be

structurally characterized. Due to its high motility, previously observed by SAXS [36], crystallographic evidence for this extra Rd domain was obtained by observing a density map assigned to its tetrahedral mononuclear Fe–Cys4 center. To complement the crystallographic data, we also obtained the NMR structure of the truncated Rd domain.

An extensive structural and molecular simulation analysis of possible substrate and product tunnels connecting the active site with the protein surface was carried out, comparing the NO-selective FIRd with the O<sub>2</sub>-selective *G. intestinalis* FDP. This revealed the presence of a tunnel of variable width crossing the diiron active site and connecting it to either side of the protein surface through a short and a long path. However, these channels reveal essentially no differences between the two proteins with opposite substrate preference. Moreover, MD calculations cannot distinguish a clear preference for either substrate in the two FDPs. Altogether, this analysis rules out a role of these channels in dictating the substrate preference in FDPs.

The structural studies reported herein further reinforce the notion that the molecular determinants of substrate specificity in the FDP family must arise from a combination of very subtle structural differences.

## Material and Methods

### Protein production

FIRd was expressed and purified as previously described [24]. For expression of the Zn-loaded Rd domain of FIRd, *E. coli* BL21(DE3)GOLD was transformed with a pT7-7-based plasmid harboring a mutated *norV* encoding a truncated FIRd comprising the residues Gly423 to Lys479 [11]. The transformed *E. coli* cells were grown until an optical density at 600 nm of 0.5, and overexpression of the Zn form of the <sup>15</sup>N-labeled Rd domain was induced with 100  $\mu$ M of IPTG as in Ref. [64]. The Rd domain was purified as previously described [65] and the NMR sample was prepared at 1.4 mM concentration in 10% D<sub>2</sub>O containing 10 mM phosphate buffer at pH 7.0.

### Crystallization of *E. coli* FIRd

Crystallization screens were set up at nL scale using a 10 mg/mL protein solution and Magic Screen (Biogenova) solutions in a Cartesian Crystallization Robot Dispensing System (Genomics Solutions) with round-bottom Greiner 96-well CrystalQuick™ plates (Greiner Bio-One). Needle-like crystals appeared in conditions #41 [0.2 M magnesium acetate tetrahydrate, 0.1 M sodium cacodylate (pH 6.5), and 20% polyethylene glycol (PEG) 8000] and #44 [0.2 M sodium acetate trihydrate, 0.1 M sodium cacodylate (pH 6.5), and 30% PEG8000]; (Magic Screen, Biogenova). These were optimized in 2- $\mu$ L sitting drops in vapor diffusion with 500- $\mu$ L reservoir solution, using XRL 24-well crystallization plates (Molecular Dimensions), at 20 °C and 30 °C and by varying the ratio of protein and crystallization solutions volumes. Further tries using the Additive Screen (Hampton Research) led to the addition of hexamine cobalt (III) chloride (condition D4), which improved the crystals' quality. The final optimized crystallization condition contained 1  $\mu$ L of 10 mg/mL of protein solution and 0.8  $\mu$ L of 0.2 M magnesium acetate, 0.2 M sodium cacodylate buffer (pH 6.5), 20% (wt/vol) PEG8000, and 0.2  $\mu$ L of 0.1 M hexamine cobalt (III) chloride at 30 °C. Cryo-protection was obtained by supplementing the mother liquor with 30% (wt/vol) glycerol. Reduced crystals were prepared by the addition of sodium dithionite powder into a drop with cryo-protected crystals under aerobic condition. The crystals became colorless and were immediately flash cryo-cooled in liquid nitrogen.

### Mass spectrometry analysis

Purified protein and redissolved protein crystal solutions were submitted to mass spectrometry analysis using a matrix-assisted laser desorption ionization time-of-flight (MALDI-TOF) mass spectrometer (APPLIED BIOSYSTEMS, model 4800).

### X-ray diffraction data collection

FIRd crystals under nitrogen at 100 K were irradiated with X-rays at the European Synchrotron Research Facility (ESRF; Grenoble, France) and Diamond Light Source (DLS; UK); diffraction images were obtained by the oscillation method. Datasets from crystals A (oxidized, as

isolated) and C (chemically reduced) were processed and scaled with XDS [66], while data from crystal B (oxidized, as isolated) were processed with HKL2000 [67].

### Structure determination, refinement, and quality assessment

Three FIRd crystal structures, from crystals A, B, and C, were determined. In crystal A, the anomalous signal of the diiron center was employed to solve the phase problem by single-wavelength anomalous diffraction using HKL2MAP GUI [68,69]. PHENIX.AUTOBUILD [70,71] was used to rebuild the initial poly-Ala chains into a unique chain with corrected amino acid sequences. The three crystal structures were refined using PHENIX.REFINE [70–72], with a preliminary rigid-body refinement cycle in the case of crystals B and C, to overcome the bias from small differences in their cell dimensions. TLSMD<sup>†</sup> [73] was used to determine the domains of translation, libration, and screw (TLS) motions. Refinement included atomic positions and *a.d.p.* optimization, refinement of TLS parameters, and automatic water solvent completion. Although refinement included standard stereochemistry libraries [74], interatomic distances involving iron centers were refined without target restraints in order to prevent prejudicial bias. Relative weights between empirical stereochemical restraints and experimental data in the minimizing function were steered by screens of  $R_{\text{free}}$  minimization. COOT [75] was used for modeling sessions of crystals structures based on their comparison against  $\sigma_A$  maps [76], leading to improvement of models and inclusion of different types of solvent molecules. These were identified by matching their shapes against those of discrete electron density blobs in  $\sigma_A$  difference maps, by comparing their refined *a.d.p.* with those of close neighbors, by checking their putative hydrogen-bonding distances with neighboring proton donors/acceptors, and, in the case of crystal A, by confirming their relative ranking of anomalous signal. Anomalous maps were produced using log-likelihood-gradient map coefficients produced by PHASER [77] in the CCP4 Suite [78]. Additionally, an iterative search for purely imaginary scatterers, to add to the real scattering model, was also generated with PHASER [77] using log-likelihood map completion. As the experimental single-wavelength anomalous diffraction maps did not show the C-terminal Rd-like domain, a BUSTER protocol designed to search for missing atoms/domains was also employed [50,51]. In order to facilitate the examination of low electron density features, absolute electron-number density scale maps were produced together with an estimation of the noise level at every map position, from maps of refinement against perturbed input data [79]. Final models' stereochemistry was assessed with MOLPROBITY [80]. SAS areas were calculated with AREAIMOL [78,81,82], and molecular surface areas with SURFACE [78,82,83]. Analysis of molecular channels was performed with COOT [75], APBS [84], and MOLE [85]. Figures of structural models and electron density maps were prepared with COOT [75] and PVMOL [86,87]. In order to produce omit maps of the active site, an initial simulated annealing step, in the case of crystal A, or an initial atom coordination shake step, in the case of crystal C (due to its lower resolution), was followed by standard PHENIX.REFINE [70–72] before map production.

### NMR structure of the FIRd Rd domain

All spectra were acquired in a Bruker AVANCE III 800 spectrometer (Bruker, Rheinstetten, Germany) working at a proton operating frequency of 800.33 MHz, equipped with a four-channel, 5-mm inverse detection probe head with pulsed field gradients along the z-axis. Spectra were run at 25 °C using standard Bruker pulse programs. Homonuclear proton correlation spectra were acquired in a phase-insensitive mode with gradient and purge pulses for coherence selection and by using an excitation sculpting scheme for water suppression. 64 transients were acquired with 4 K complex points and 1 K increments over a 16 × 16 ppm sweep width, with a recycle delay of 0.65 s. Nuclear Overhauser enhancement spectroscopy (NOESY) and total correlation spectra (TOCSY) were acquired using gradient pulses for coherence selection and an excitation sculpting scheme for water suppression in the phase-sensitive mode using States-TPP1. Over a 16 × 16 ppm sweep width centered at 4.70 ppm, 96 transients were acquired with 4 K complex points and 256 increments, with a recycle delay of 1.65 s and 3.15 s for the NOESY and the TOCSY, respectively. The TOCSY spectra used a DIPSY2 scheme for mixing, with mixing times of 70 and 20 ms. The NOESY spectra were acquired with an 80-ms mixing time.

In the <sup>1</sup>H–<sup>15</sup>N heteronuclear single quantum coherence (HSQC) spectrum, a delay of 5.55 ms was used for the evolution of <sup>1</sup>J<sub>NH</sub>. Gradient pulses were used during the inverse INEPT sequence for selection, together with adiabatic shaped pulses for inversion. With a recycle delay of 1.15 s, 4 transients were acquired with 4 K complex points and 256 increments over a 16 × 45 ppm sweep width. Proton decoupling was achieved using the GARP4 sequence [88].

The 3D <sup>1</sup>H–<sup>15</sup>N HSQC-TOCSY spectrum was acquired with 16 transients and 4 K × 48 × 180 points over a sweep width of 16 × 48 × 11 ppm using the same parameters as in the 2D HSQC and TOCSY spectra described above. Peaks were assigned, and NOE peak volumes were measured from the 2D <sup>1</sup>H NOESY spectrum with an 80-ms mixing time spectrum using lineshape fitting with the software SPARKY [89]. For each calculation cycle, 500 structures were produced with 40,000 simulated annealing steps using the program DYANA [90], modified to accept peak volumes as constraints, as discussed in Ref. [91]. The 20 structures with the lowest target functions were chosen to represent the structure. Structures were analyzed with the program PROCHECK-NMR [92].

### Amino acid sequence alignments based on 3D structures

3D multibody superposition of polypeptide chains was performed with MODELLER [93].

### Molecular modeling – system preparation

O<sub>2</sub> and NO diffusion MD simulations were performed using the *E. coli* FIRd crystallographic structure (Crystal A) in this work and the *G. intestinalis* FDP structure (PDB code 2Q9U). This analysis was restricted to the flavodiiron core (head-to-tail homodimer) of both structures. In the structure of *G. intestinalis* FDP, the side chains of several residues had to be fitted to alanine residues due to the lack

of electron density. Two strategies for correcting these missing coordinates were followed; in the first, the complete side chains of one monomer were added to the other monomer, where these were missing (fitting both monomers). In the second, the missing side chains from both monomers were added to the structure using the PyMol Mutagenesis Tool (v.0.99, Schrödinger, LLC). The residues' protonation state in the two proteins was simulated using continuum electrostatics, which is used to calculate individual energetic terms that are then applied in a Monte Carlo method to estimate the joint protonation probability of individual residues at a given pH value. The protein and solvent were treated as two distinct dielectric media, and the system is described by the linear form of the Poisson–Boltzmann equation. The Poisson–Boltzmann calculations were performed with MEAD [96], and the Monte Carlo sampling was performed with PETIT, as previously described [97–99]. From the obtained protonation profile, the predominant protonation state of each residue at pH 7 was considered in the MD simulations.

The GROMOS 53A6 force field charge set [100] was used to assign the atomic partial charges for the protein residues and FMN coenzyme. The charges of the diiron center's first coordination sphere residues were assigned based on quantum calculations performed with Gaussian 98 [101], using B3LYP and the 6-31G(d) basis set for organic atoms and the 6-31G(3df) basis set for the two iron atoms (which were considered to be uncoupled). The results were used to generate electrostatic potentials, which were fitted with the restrained electrostatic potential procedure [102]. As previously described for *D. gigas* FDP, both FMN and diiron center were considered to be in the reduced state [41]. The initial topology was corrected to incorporate all the necessary bonds, angles, and dihedrals of the diiron catalytic center using an in-house software (fix\_topology). All MD simulations were done using the GROMACS version 4.0.4 [103].

### Molecular modeling – MD protocol

For each protein, we have initially performed six replicate MD simulations in pure water in order to equilibrate both systems for subsequent MD simulations in the presence of both O<sub>2</sub> and NO. We have started with a minimization in vacuum using the L-BFGS method in double precision. The initial step size was of 0.001 nm, totaling 2000 steps of minimization with 10 correction steps. For each 1000 steps of L-BFGS, one step of steepest descent was performed. Non-bonded interactions were calculated with a twin range method [104], with short and long range cutoffs of 8 and 14 Å, respectively. A reaction field correction was applied to electrostatic interactions [105,106], considering a dielectric constant of 54, the dielectric constant of single point charge (SPC) water [107]. The minimized structure was solvated on a dodecahedral box with SPC water [108], considering a minimum distance of 0.9 nm between the protein and box walls. The system was then minimized using the same procedure previously described.

Minimized structures were used as the starting point for the all MD simulations. The initialization of these simulations comprised three steps. Prior to the initialization steps themselves, the initial velocities were generated independently for each of the six replicates. The initialization steps comprised three stretches of 50 ps with a Berendsen temperature bath at

300 K, with independent coupling between protein and water, and a Berendsen pressure coupling at 1 atm. The first stretch used position restraints on all heavy atoms, had a temperature coupling constant of 0.01 ps, and was performed at constant volume. The second stretch introduced pressure coupling with a coupling constant of 0.5 ps. The final stretch of initialization restrained Ca atoms only, and the temperature coupling was loosened to a coupling constant of 0.1 ps. The production runs freed the system of all position restraints and covered a simulation time of 20 ns.

The structures of the last frame of each replicate simulation were used as the starting point of the next set of simulations, now integrating NO and O<sub>2</sub> molecules. Then, 200 NO and O<sub>2</sub> molecules were randomly placed outside of the protein in a way to avoid clashes with water molecules. The NO and O<sub>2</sub> parameters were taken from Ref. [41]. Although the system's NO and O<sub>2</sub> concentrations used in this work are above their natural solubility, this was necessary to guarantee sufficient sampling within a reasonable simulation time [41]. Each pair of replicates, solvated with either NO and O<sub>2</sub>, had the same number of atoms and atomic coordinates. Prior to the MD simulations themselves, each individual replicate was minimized with the steepest descent method. The initial step size was 0.001 nm, totaling 2000 steps of minimization, with a conjugate gradient step for every 1000 steps of steepest descent. The minimized systems were then prepared for MD with the same protocol used for the MD simulations described in the previous section. Water molecules covering the inner cavities of the protein were removed to avoid a possible compromise of the diffusion pathways. An additional temperature coupling group was used for the NO or O<sub>2</sub> molecules. Each MD simulation replicate was performed for 30 ns.

### Molecular modelling – free energy calculations

To evaluate which of the studied molecules had greater affinity for the catalytic center pocket of both *E. coli* FIRd and *G. intestinalis* FDP, we used a free energy thermodynamic cycle [109]. To apply this method to the system under the study, we have started by defining the closed thermodynamic cycle (see Fig. 3 in Ref. [41]), followed by the two non-chemical conversions of NO into O<sub>2</sub> ( $\Delta G_3$  and  $\Delta G_4$ ) in solution (three replicate simulations) and inside the diiron catalytic site of the proteins (six replicate simulations). In the end, it is possible to calculate the relative binding free energy of O<sub>2</sub> and NO to the *G. intestinalis* and *E. coli* FDPs using the thermodynamic integration method [110] and the following expression:  $\Delta\Delta G = \Delta G_2 - \Delta G_1 = \Delta G_4 - \Delta G_3$ .

The initial protein structures used in the simulations were obtained from the 20-ns-long water equilibration simulations. We used 11 equally spaced  $\lambda$  steps to convert NO into O<sub>2</sub> in the diiron catalytic site. Each step consisted of 100 ps of equilibration, followed by 600 ps of production. For the conversion of the molecules in water, the system consisted of a NO molecule inside a 3.0-nm<sup>3</sup> water box containing 966 water molecules. The procedure was initiated with 1 ns of equilibration, followed by 21 equally spaced  $\lambda$  steps. Each individual  $\lambda$  step consisted of 400 ps of equilibration and 2 ns of production. The bonded potentials were linearly interpolated, while the non-bonded interactions were interpolated via soft-core interactions, with parameter  $\alpha$  equal to 0.1 and  $\lambda$  power  $p$  equal to 2. The remaining parameters

followed the ones used for the production runs of the FDPs on water.

### Accession Numbers

The crystallographic and NMR data were deposited in the Protein Data Bank [94,95]. The coordinates and structure factors of the crystal structures have been deposited with the following accession codes: 4D02 (FIRd in the isolated state, crystal A), 5LMC (FIRd with [Fe–4S<sup>G</sup>] from Rd domain, crystal B), and 5LLD (FIRd in the reduced state, crystal C; Table 3). The 20 NMR structures with the lowest target functions of the Rd domain have been deposited with the accession code 2MS3 (Table 3). Although the Rd domain structure was deposited with the amino acid residue numbering from residue 1 (Gly) to 57 (Lys), in the present manuscript, the numbering of the full-length FIRd, residues Gly423 to Lys479 was used.

### Acknowledgments

This work was financed by the Portuguese Fundação para a Ciência e Tecnologia (FCT) through grant PTDC/BBB-BQB/3135/2014 (M.T.). C.V.R. and P.T.B. acknowledge the FCT grants SFRH/BPD/94050/2013 and SFRH/BD/85106/2012. J.B.V. is an FCT Investigator (IF/01004/2014). This work was further financially supported by MOSTMICRO (LISBOA-01-0145-FEDER-007660), by iNOVA4Health (LISBOA-01-0145-FEDER-007344) Research Units co-funded by FCT, through national funds, and by FEDER under the PT2020 Partnership Agreement. The NMR spectrometers are part of the Portuguese National NMR Facility (RECI/BBB-BQB/0230/2012) supported by FCT. Mass spectrometry data were provided by the UniMS - Mass Spectrometry Unit, ITQB/iBET, Oeiras, Portugal. We thank the beamline staff at ESRF (Grenoble, France) and DLS (UK) for the support during the synchrotron data collections, and F. Folgosa and M. Martins for the critical reading of the manuscript.

Received 1 August 2016;

Received in revised form 2 October 2016;

Accepted 4 October 2016

Available online 7 October 2016

### Keywords:

flavorubredoxin;  
flavodiiron protein;  
NorV;  
diiron center;  
nitric oxide

Present address: B.L. Victor, Centro de Química e Bioquímica, Departamento de Química e Bioquímica, Faculdade de Ciências, Universidade de Lisboa, 1749-016 Lisboa, Portugal.

†<http://skuld.bmsc.washington.edu/~tismd>

#### Abbreviations used:

NO, nitric oxide; Hmp, flavohaemoglobin; FIRd, flavorubredoxin; FDP, flavodiiron protein; FMN, flavin mononucleotide; Rd, rubredoxin; MD, molecular dynamics; SAXS, small-angle X-ray scattering; *a.u.*, asymmetric unit; SAS, solvent-accessible surface; *a.d.p.*, atomic displacement parameter;  $\mu\text{-OH}^\ominus$ ,  $\mu\text{-hydroxo}$ ; PEG, polyethylene glycol; ESRF, European Synchrotron Research Facility; DLS, Diamond Light Source; TLS, translation, libration, and screw; NOESY, Nuclear Overhauser enhancement spectroscopy; TOCSY, total correlation spectra; HSQC, heteronuclear single quantum coherence; SPC, single point charge.

## References

- [1] J. MacMicking, Q.W. Xie, C. Nathan, Nitric oxide and macrophage function, *Annu. Rev. Immunol.* 15 (1997) 323–350.
- [2] F.C. Fang, Antimicrobial reactive oxygen and nitrogen species: concepts and controversies, *Nat. Rev. Microbiol.* 2 (2004) 820–832.
- [3] L.R. Jarboe, D.R. Hyduke, J.C. Liao, Systems Approaches to Unraveling Nitric Oxide Response Networks in Prokaryotes, in: L.J. Ignarro (Ed.) *Nitric oxide : biology and pathobiology* (2nd Edit) Academic Press, San Diego, California, USA 2010, pp. 103–136.
- [4] C. Bogdan, Nitric oxide and the immune response, *Nat. Immunol.* 2 (2001) 907–916.
- [5] R.K. Poole, M.N. Hughes, New functions for the ancient globin family: bacterial responses to nitric oxide and nitrosative stress, *Mol. Microbiol.* 36 (2000) 775–783.
- [6] A. Hausladen, A. Gow, J.S. Stamler, Flavohemoglobin denitrosylase catalyzes the reaction of a nitroxyl equivalent with molecular oxygen, *Proc. Natl. Acad. Sci. U. S. A.* 98 (2001) 10,108–10,112.
- [7] S.R. Pooch, E.R. Leach, J.W. Moir, J.A. Cole, D.J. Richardson, Respiratory detoxification of nitric oxide by the cytochrome c nitrite reductase of *Escherichia coli*, *J. Biol. Chem.* 277 (2002) 23,664–23,669.
- [8] C.E. Vine, J.A. Cole, Unresolved sources, sinks, and pathways for the recovery of enteric bacteria from nitrosative stress, *FEMS Microbiol. Lett.* 325 (2011) 99–107.
- [9] C. Costa, A. Macedo, I. Moura, J.J. Moura, J. Le Gall, Y. Berlier, M.Y. Liu, W.J. Payne, Regulation of the hexaheme nitrite/nitric oxide reductase of *Desulfovibrio desulfuricans*, *Wolinella succinogenes* and *Escherichia coli*. A mass spectrometric study, *FEBS Lett.* 276 (1990) 67–70.
- [10] A.M. Gardner, R.A. Helmick, P.R. Gardner, Flavorubredoxin, an inducible catalyst for nitric oxide reduction and detoxification in *Escherichia coli*, *J. Biol. Chem.* 277 (2002) 8172–8177.
- [11] C.M. Gomes, A. Giuffre, E. Forte, J.B. Vicente, L.M. Saraiva, M. Brunori, M. Teixeira, A novel type of nitric-oxide reductase. *Escherichia coli* flavorubredoxin, *J. Biol. Chem.* 277 (2002) 25,273–25,276.
- [12] J. Wang, C.E. Vine, B.K. Balasiny, J. Rizk, C.L. Bradley, M.T. Trejo, R.K. Poole, L.L. Bergaust, L.R. Bakken, J.A. Cole, The roles of the hybrid cluster protein, Hcp, and its reductase, Hcr, in high affinity nitric oxide reduction that protects anaerobic cultures of *Escherichia coli* against nitrosative stress, *Mol. Microbiol.* 100 (2016) 877–892.
- [13] J.B. Vicente, F.M. Scandurra, E. Forte, M. Brunori, P. Sarti, M. Teixeira, A. Giuffre, Kinetic characterization of the *Escherichia coli* nitric oxide reductase flavorubredoxin, *Methods Enzymol.* 437 (2008) 47–62.
- [14] D.R. Hyduke, L.R. Jarboe, L.M. Tran, K.J. Chou, J.C. Liao, Integrated network analysis identifies nitric oxide response networks and dihydroxyacid dehydratase as a crucial target in *Escherichia coli*, *Proc. Natl. Acad. Sci. U. S. A.* 104 (2007) 8484–8489.
- [15] M.C. Justino, J.B. Vicente, M. Teixeira, L.M. Saraiva, New genes implicated in the protection of anaerobically grown *Escherichia coli* against nitric oxide, *J. Biol. Chem.* 280 (2005) 2636–2643.
- [16] S.T. Pullan, M.D. Gidley, R.A. Jones, J. Barrett, T.M. Stevanin, R.C. Read, J. Green, R.K. Poole, Nitric oxide in chemostat-cultured *Escherichia coli* is sensed by Fnr and other global regulators: unaltered methionine biosynthesis indicates lack of S nitrosation, *J. Bacteriol.* 189 (2007) 1845–1855.
- [17] H.H. Mehta, Y. Liu, M.Q. Zhang, S. Spiro, Genome-wide analysis of the response to nitric oxide in uropathogenic *Escherichia coli* CFT073, *Microbial Genomics* 1 (2015), <http://dx.doi.org/10.1099/mgen.0.000031>.
- [18] J.M. Baptista, M.C. Justino, A.M. Melo, M. Teixeira, L.M. Saraiva, Oxidative stress modulates the nitric oxide defense promoted by *Escherichia coli* flavorubredoxin, *J. Bacteriol.* 194 (2012) 3611–3617.
- [19] T. Shimizu, H. Tsutsuki, A. Matsumoto, H. Nakaya, M. Noda, The nitric oxide reductase of enterohaemorrhagic *Escherichia coli* plays an important role for the survival within macrophages, *Mol. Microbiol.* 85 (2012) 492–512.
- [20] B.R. Kulasekara, M. Jacobs, Y. Zhou, Z. Wu, E. Sims, C. Saenphimmachak, L. Rohmer, J.M. Ritchie, M. Radey, M. McKeivitt, T.L. Freeman, H. Hayden, E. Haugen, W. Gillett, C. Fong, J. Chang, V. Beskhebnaya, M.K. Waldor, M. Samadpour, T.S. Whittam, R. Kaul, M. Brittnacher, S.I. Miller, Analysis of the genome of the *Escherichia coli* O157: H7 2006 spinach-associated outbreak isolate indicates candidate genes that may enhance virulence, *Infect. Immun.* 77 (2009) 3713–3721.
- [21] A. Wasserfallen, S. Ragetti, Y. Jouanneau, T. Leisinger, A family of flavoproteins in the domains Archaea and Bacteria, *Eur. J. Biochem.* 254 (1998) 325–332.
- [22] C.V. Romao, J.B. Vicente, P.T. Borges, C. Frazao, M. Teixeira, The dual function of flavodiiron proteins: oxygen and/or nitric oxide reductases, *J. Biol. Inorg. Chem.* 21 (2016) 39–52.
- [23] J.B. Vicente, F.M. Scandurra, J.V. Rodrigues, M. Brunori, P. Sarti, M. Teixeira, A. Giuffre, Kinetics of electron transfer from NADH to the *Escherichia coli* nitric oxide reductase flavorubredoxin, *FEBS J.* 274 (2007) 677–686.
- [24] J.B. Vicente, M. Teixeira, Redox and spectroscopic properties of the *Escherichia coli* nitric oxide-detoxifying system involving flavorubredoxin and its NADH-oxidizing redox partner, *J. Biol. Chem.* 280 (2005) 34,599–34,608.
- [25] C.M. Gomes, J.B. Vicente, A. Wasserfallen, M. Teixeira, Spectroscopic studies and characterization of a novel electron-transfer chain from *Escherichia coli* involving a flavorubredoxin and its flavoprotein reductase partner, *Biochemistry* 39 (2000) 16,230–16,237.

- [26] A. Di Matteo, F.M. Scandurra, F. Testa, E. Forte, P. Sarti, M. Brunori, A. Giuffrè, The O<sub>2</sub>-scavenging flavodiiron protein in the human parasite *Giardia intestinalis*, *J. Biol. Chem.* 283 (2008) 4061–4068.
- [27] T. Smutna, V.L. Goncalves, L.M. Saraiva, J. Tachezy, M. Teixeira, I. Hrdy, Flavodiiron protein from *Trichomonas vaginalis* hydrogenosomes: the terminal oxygen reductase, *Eukaryot. Cell* 8 (2009) 47–55.
- [28] J.B. Vicente, V. Tran, L. Pinto, M. Teixeira, U. Singh, A detoxifying oxygen reductase in the anaerobic protozoan *Entamoeba histolytica*, *Eukaryot. Cell* 11 (2012) 1112–1118.
- [29] P. Zhang, Y. Allahverdiyeva, M. Eisenhut, E.M. Aro, Flavodiiron proteins in oxygenic photosynthetic organisms: photoprotection of photosystem II by Flv2 and Flv4 in *Synechocystis* sp. PCC 6803, *PLoS One* 4 (2009), e5331.
- [30] V.L. Gonçalves, L.M. Saraiva, M. Teixeira, Gene expression study of the flavodi-iron proteins from the cyanobacterium *Synechocystis* sp. PCC6803, *Biochem. Soc. Trans.* 39 (2011) 216–218.
- [31] J.B. Vicente, C.M. Gomes, A. Wasserfallen, M. Teixeira, Module fusion in an A-type flavoprotein from the cyanobacterium *Synechocystis* condenses a multiple-component pathway in a single polypeptide chain, *Biochem. Biophys. Res. Commun.* 294 (2002) 82–87.
- [32] H. Yamamoto, S. Takahashi, M.R. Badger, T. Shikanai, Artificial remodelling of alternative electron flow by flavodiiron proteins in *Arabidopsis*, *Nat. Plants* 2 (2016) 16,012.
- [33] J.B. Vicente, M.A. Carrondo, M. Teixeira, C. Frazão, Flavodiiron proteins: nitric oxide and/or oxygen reductases, *Handbook of Metalloproteins*, vol. 1, John Wiley & Sons, Ltd., 2007 (<http://onlinelibrary.wiley.com/doi/10.1002/0470028637.met218/abstract>).
- [34] V.L. Gonçalves, J.B. Vicente, L.M. Saraiva, M. Teixeira, Flavodiiron Proteins and their role in cyanobacteria, in: G.A. Peschek, C. Obinger, G. Renger (Eds.), *Bioenergetic Processes of cyanobacteria- From Evolutionary Singularity to Ecological Diversity*, 1st Ed, Chap. 22, Springer Verlag, Springer, Netherlands 2011, pp. 631–655.
- [35] L.M. Saraiva, J.B. Vicente, M. Teixeira, The role of the flavodiiron proteins in microbial nitric oxide detoxification, *Adv. Microb. Physiol.* 49 (2004) 77–129.
- [36] M.V. Petoukhov, J.B. Vicente, P.B. Crowley, M.A. Carrondo, M. Teixeira, D.I. Svergun, Quaternary structure of flavorubredoxin as revealed by synchrotron radiation small-angle X-ray scattering, *Structure* 16 (2008) 1428–1436.
- [37] H. Seedorf, A. Dreisbach, R. Hedderich, S. Shima, R.K. Thauer, F420H2 oxidase (FprA) from *Methanobrevibacter arborophilus*, a coenzyme F420-dependent enzyme involved in O<sub>2</sub> detoxification, *Arch. Microbiol.* 182 (2004) 126–137.
- [38] R. Rodrigues, J.B. Vicente, R. Felix, S. Oliveira, M. Teixeira, C. Rodrigues-Pousada, *Desulfovibrio gigas* flavodiiron protein affords protection against nitrosative stress *in vivo*, *J. Bacteriol.* 188 (2006) 2745–2751.
- [39] R. Silaghi-Dumitrescu, E.D. Coulter, A. Das, L.G. Ljungdahl, G.N. Jameson, B.H. Huynh, D.M. Kurtz Jr., A flavodiiron protein and high molecular weight rubredoxin from *Moorella thermoacetica* with nitric oxide reductase activity, *Biochemistry* 42 (2003) 2806–2815.
- [40] R. Silaghi-Dumitrescu, D.M. Kurtz Jr., L.G. Ljungdahl, W.N. Lanzilotta, X-ray crystal structures of *Moorella thermoacetica* FprA. Novel diiron site structure and mechanistic insights into a scavenging nitric oxide reductase, *Biochemistry* 44 (2005) 6492–6501.
- [41] B.L. Victor, A.M. Baptista, C.M. Soares, Dioxygen and nitric oxide pathways and affinity to the catalytic site of rubredoxin:oxygen oxidoreductase from *Desulfovibrio gigas*, *J. Biol. Inorg. Chem.* 14 (2009) 853–862.
- [42] L. Chen, M.Y. Liu, J. LeGall, P. Fareleira, H. Santos, A.V. Xavier, Rubredoxin oxidase, a new flavo-hemo-protein, is the site of oxygen reduction to water by the “strict anaerobe” *Desulfovibrio gigas*, *Biochem. Biophys. Res. Commun.* 193 (1993) 100–105.
- [43] H. Seedorf, C.H. Hagemeyer, S. Shima, R.K. Thauer, E. Warkentin, U. Ermler, Structure of coenzyme F420H2 oxidase (FprA), a di-iron flavoprotein from methanogenic Archaea catalyzing the reduction of O<sub>2</sub> to H<sub>2</sub>O, *FEBS J.* 274 (2007) 1588–1599.
- [44] M. Harding, The geometry of metal–ligand interactions relevant to proteins, *Acta Crystallogr. Sect. D* 55 (1999) 1432–1443.
- [45] R.P. Joosten, F. Long, G.N. Murshudov, A. Perrakis, The PDB\_REDO server for macromolecular structure model optimization, *IUCrJ* 1 (2014) 213–220.
- [46] C.M. Gomes, G. Silva, S. Oliveira, J. LeGall, M.Y. Liu, A.V. Xavier, C. Rodrigues-Pousada, M. Teixeira, Studies on the redox centers of the terminal oxidase from *Desulfovibrio gigas* and evidence for its interaction with rubredoxin, *J. Biol. Chem.* 272 (1997) 22,502–22,508.
- [47] V.L. Gonçalves, J.B. Vicente, L. Pinto, C.V. Romão, C. Frazão, P. Sarti, A. Giuffrè, M. Teixeira, Flavodiiron oxygen reductase from *Entamoeba histolytica*: modulation of substrate preference by tyrosine 271 and lysine 53, *J. Biol. Chem.* 289 (2014) 28,260–28,270.
- [48] J.B. Vicente, F. Testa, D. Mastronicola, E. Forte, P. Sarti, M. Teixeira, A. Giuffrè, Redox properties of the oxygen-detoxifying flavodiiron protein from the human parasite *Giardia intestinalis*, *Arch. Biochem. Biophys.* 488 (2009) 9–13.
- [49] Y. Jouanneau, C. Meyer, M. Asso, B. Guigliarelli, J.C. Willison, Characterization of a nif-regulated flavoprotein (FprA) from *Rhodobacter capsulatus*. Redox properties and molecular interaction with a [2Fe-2S] ferredoxin, *Eur. J. Biochem.* 267 (2000) 780–787.
- [50] E. Blanc, P. Roversi, C. Vornrhein, C. Flensburg, S.M. Lea, G. Bricogne, Refinement of severely incomplete structures with maximum likelihood in BUSTER-TNT, *Acta Crystallogr. D Biol. Crystallogr.* 60 (2004) 2210–2221.
- [51] P. Roversi, E. Blanc, C. Vornrhein, G. Evans, G. Bricogne, Modelling prior distributions of atoms for macromolecular refinement and completion, *Acta Crystallogr. D Biol. Crystallogr.* 56 (2000) 1316–1323.
- [52] C.J. Chen, Y.H. Lin, Y.C. Huang, M.Y. Liu, Crystal structure of rubredoxin from *Desulfovibrio gigas* to ultra-high 0.68 Å resolution, *Biochem. Biophys. Res. Commun.* 349 (2006) 79–90.
- [53] M.K. Eidsness, A.E. Burden, K.A. Richie, D.M. Kurtz Jr., R.A. Scott, E.T. Smith, T. Ichiye, B. Beard, T. Min, C. Kang, Modulation of the redox potential of the [Fe(SCys)<sub>4</sub>] site in rubredoxin by the orientation of a peptide dipole, *Biochemistry* 38 (1999) 14,803–14,809.
- [54] I. Moura, J.J. Moura, M.H. Santos, A.V. Xavier, J. Le Gall, Redox studies on rubredoxins from sulphate and sulphur reducing bacteria, *FEBS Lett.* 107 (1979) 419–421.
- [55] J. LeGall, M.Y. Liu, C.M. Gomes, V. Braga, I. Pacheco, M. Regalla, A.V. Xavier, M. Teixeira, Characterisation of a new rubredoxin isolated from *Desulfovibrio desulfuricans* 27774:

- definition of a new family of rubredoxins, *FEBS Lett.* 429 (1998) 295–298.
- [56] F. Auchere, R. Sikkink, C. Cordas, P. Raleiras, P. Tavares, I. Moura, J.J. Moura, Overexpression and purification of *Treponema pallidum* rubredoxin; kinetic evidence for a superoxide-mediated electron transfer with the superoxide reductase neelaredoxin, *J. Biol. Inorg. Chem.* 9 (2004) 839–849.
- [57] M.W.W. Adams, Novel iron–sulfur centers in metalloenzymes and redox proteins from extremely thermophilic bacteria, in: R. Cammack (Ed.) *Advances in Inorganic Chemistry*, vol. 38, Academic Press, London, 1992, pp. 341–396.
- [58] M. Ayhan, Z. Xiao, M.J. Lavery, A.M. Hamer, K.W. Nugent, S.D.B. Scrofanì, M. Guss, A.G. Wedd, The rubredoxin from *Clostridium pasteurianum*: mutation of the conserved glycine residues 10 and 43 to alanine and valine, *Inorg. Chem.* 35 (1996) 5902–5911.
- [59] Z. Xiao, M.J. Maher, M. Cross, C.S. Bond, J.M. Guss, A.G. Wedd, Mutation of the surface valine residues 8 and 44 in the rubredoxin from *Clostridium pasteurianum*: solvent access versus structural changes as determinants of reversible potential, *J. Biol. Inorg. Chem.* 5 (2000) 75–84.
- [60] Q. Zeng, E.T. Smith, D.M. Kurtz Jr., R.A. Scott, Protein determinants of metal site reduction potentials: site-directed mutagenesis studies of *Clostridium pasteurianum* rubredoxin, *Inorg. Chim. Acta* 242 (1996) 245–251.
- [61] R. Kummerle, H. Zhuang-Jackson, J. Gaillard, J.M. Moulis, Site-directed mutagenesis of rubredoxin reveals the molecular basis of its electron transfer properties, *Biochemistry* 36 (1997) 15,983–15,991.
- [62] H.B. Gray, J.R. Winkler, Hole hopping through tyrosine/tryptophan chains protects proteins from oxidative damage, *Proc. Natl. Acad. Sci. U. S. A.* 112 (2015) 10,920–10,925.
- [63] N.F. Polizzi, A. Migliore, M.J. Therien, D.N. Beratan, Defusing redox bombs? *Proc. Natl. Acad. Sci. U. S. A.* 112 (2015) 10,821–10,822.
- [64] P. Lamosa, D.L. Turner, R. Ventura, C. Maycock, H. Santos, Protein stabilization by compatible solutes. Effect of diglycerol phosphate on the dynamics of *Desulfovibrio gigas* rubredoxin studied by NMR, *Eur. J. Biochem.* 270 (2003) 4606–4614.
- [65] P. Lamosa, A. Burke, R. Peist, R. Huber, M.Y. Liu, G. Silva, C. Rodrigues-Pousada, J. LeGall, C. Maycock, H. Santos, Thermostabilization of proteins by diglycerol phosphate, a new compatible solute from the hyperthermophile *Archaeoglobus fulgidus*, *Appl. Environ. Microbiol.* 66 (2000) 1974–1979.
- [66] W. Kabsch, Xds, *Acta Crystallogr. D Biol. Crystallogr.* 66 (2010) 125–132.
- [67] Z. Otwinowski, W. Minor, Processing of X-ray diffraction data collected in oscillation mode, in: C.W. Carter Jr., R.M. Sweet (Eds.), *Methods in Enzymology, Macromolecular Crystallography*, part A, Vol. 276, Academic Press, New York 1997, pp. 307–326.
- [68] T. Pape, T.R. Schneider, HKL2MAP: a graphical user interface for macromolecular phasing with SHELX programs, *J. Appl. Crystallogr.* 37 (2004) 843–844.
- [69] G.M. Sheldrick, A short history of SHELX, *Acta Crystallogr. A* 64 (2008) 112–122.
- [70] P.D. Adams, P.V. Afonine, G. Bunkoczi, V.B. Chen, I.W. Davis, N. Echols, J.J. Headd, L.W. Hung, G.J. Kapral, R.W. Grosse-Kunstleve, A.J. McCoy, N.W. Moriarty, R. Oeffner, R.J. Read, D.C. Richardson, J.S. Richardson, T.C. Terwilliger, P.H. Zwart, PHENIX: a comprehensive Python-based system for macromolecular structure solution, *Acta Crystallogr. D Biol. Crystallogr.* 66 (2010) 213–221.
- [71] T.C. Terwilliger, R.W. Grosse-Kunstleve, P.V. Afonine, N.W. Moriarty, P.H. Zwart, L.W. Hung, R.J. Read, P.D. Adams, Iterative model building, structure refinement and density modification with the PHENIX AutoBuild wizard, *Acta Crystallogr. D Biol. Crystallogr.* 64 (2008) 61–69.
- [72] P.V. Afonine, R.W. Grosse-Kunstleve, N. Echols, J.J. Headd, N.W. Moriarty, M. Mustyakimov, T.C. Terwilliger, A. Urzhumtsev, P.H. Zwart, P.D. Adams, Towards automated crystallographic structure refinement with phenix.refine, *Acta Crystallogr. D Biol. Crystallogr.* 68 (2012) 352–367.
- [73] J. Painter, E.A. Merritt, Optimal description of a protein structure in terms of multiple groups undergoing TLS motion, *Acta Crystallogr. D Biol. Crystallogr.* 62 (2006) 439–450.
- [74] R.A. Engh, R. Huber, Accurate Bond and Angle Parameters for X-Ray Protein-Structure Refinement, *Acta Crystallogr. A* 47 (1991) 392–400.
- [75] P. Emsley, B. Lohkamp, W.G. Scott, K. Cowtan, Features and development of Coot, *Acta Crystallogr. D Biol. Crystallogr.* 66 (2010) 486–501.
- [76] R.J. Read, Improved Fourier coefficients for maps using phases from partial structures with errors, *Acta Crystallogr. A* 42 (1986) 140–149.
- [77] A.J. McCoy, R.W. Grosse-Kunstleve, P.D. Adams, M.D. Winn, L.C. Storoni, R.J. Read, Phaser crystallographic software, *J. Appl. Crystallogr.* 40 (2007) 658–674.
- [78] M.D. Winn, C.C. Ballard, K.D. Cowtan, E.J. Dodson, P. Emsley, P.R. Evans, R.M. Keegan, E.B. Krissinel, A.G.W. Leslie, A. McCoy, S.J. McNicholas, G.N. Murshudov, N.S. Pannu, E.A. Potterton, H.R. Powell, R.J. Read, A. Vagin, K.S. Wilson, Overview of the CCP4 suite and current developments, *Acta Crystallogr. D Biol. Crystallogr.* 67 (2011) 235–242.
- [79] P.T. Lang, J.M. Holton, J.S. Fraser, T. Alber, Protein structural ensembles are revealed by redefining X-ray electron density noise, *Proc. Natl. Acad. Sci. U. S. A.* 111 (2014) 237–242.
- [80] I.W. Davis, A. Leaver-Fay, V.B. Chen, J.N. Block, G.J. Kapral, X. Wang, L.W. Murray, W.B. Arendall, J. Snoeyink, J.S. Richardson, D.C. Richardson, MolProbity: all-atom contacts and structure validation for proteins and nucleic acids, *Nucleic Acids Res.* 35 (2007) W375–W383.
- [81] E. Krissinel, K. Henrick, Inference of macromolecular assemblies from crystalline state, *J. Mol. Biol.* 372 (2007) 774–797.
- [82] B. Lee, F.M. Richards, Interpretation of protein structures—estimation of static accessibility, *J. Mol. Biol.* 55 (1971) 379–400.
- [83] C. Chothia, Structural invariants in protein folding, *Nature* 254 (1975) 304–308.
- [84] N.A. Baker, D. Sept, S. Joseph, M.J. Holst, J.A. McCammon, Electrostatics of nanosystems: application to microtubules and the ribosome, *Proc. Natl. Acad. Sci. U. S. A.* 98 (2001) 10,037–10,041.
- [85] D. Sehnal, R. Svobodova Varekova, K. Berka, L. Pravda, V. Navratilova, P. Banas, C.M. Ionescu, M. Otyepka, J. Koca, MOLE 2.0: advanced approach for analysis of biomacromolecular channels, *J. Cheminform.* 5 (2013) 39.
- [86] W.L. DeLano, The PyMOL Molecular Graphics System, 2002.
- [87] L.L.C. Schrodinger, The PyMOL Molecular Graphics System, Version 1.3r1, 2010.
- [88] A.J. Shaka, P.B. Barker, R. Freeman, Computer-optimized decoupling scheme for wideband applications and low-level operation, *J. Magn. Reson.* 64 (1985) 547–552.

- [89] T.D. Goddard, D.G. Kneller. SPARKY 3. University of California, San Francisco.
- [90] P. Guntert, C. Mumenthaler, K. Wuthrich, Torsion angle dynamics for NMR structure calculation with the new program DYANA, *J. Mol. Biol.* 273 (1997) 283–298.
- [91] V.B. Paixao, H. Vis, D.L. Turner, Redox linked conformational changes in cytochrome c3 from *Desulfovibrio desulfuricans* ATCC 27774, *Biochemistry* 49 (2010) 9620–9629.
- [92] R.A. Laskowski, J.A. Rullmann, M.W. MacArthur, R. Kaptein, J.M. Thornton, AQUA and PROCHECK-NMR: programs for checking the quality of protein structures solved by NMR, *J. Biomol. NMR* 8 (1996) 477–486.
- [93] B. Webb, A. Sali, Protein structure modeling with MODELLER, *Methods Mol. Biol.* 1137 (2014) 1–15.
- [94] S. Velankar, Y. Alhroub, C. Best, S. Caboche, M.J. Conroy, J.M. Dana, M.A. Fernandez Montecelo, G. van Ginkel, A. Golovin, S.P. Gore, A. Gutmanas, P. Haslam, P.M. Hendrickx, E. Heuson, M. Hirshberg, M. John, I. Lagerstedt, S. Mir, L.E. Newman, T.J. Oldfield, A. Patwardhan, L. Rinaldi, G. Sahni, E. Sanz-Garcia, S. Sen, R. Slowley, A. Suarez-Uruena, G.J. Swaminathan, M.F. Symmons, W.F. Vranken, M. Wainwright, G.J. Kleywegt, PDB: Protein Data Bank in Europe, *Nucleic Acids Res.* 40 (2012) D445–D452.
- [95] H.M. Berman, J. Westbrook, Z. Feng, G. Gilliland, T.N. Bhat, H. Weissig, I.N. Shindyalov, P.E. Bourne, The Protein Data Bank, *Nucleic Acids Res.* 28 (2000) 235–242.
- [96] D. Bashford, K. Gerwert, Electrostatic calculations of the pKa values of ionizable groups in bacteriorhodopsin, *J. Mol. Biol.* 224 (1992) 473–486.
- [97] A.M. Baptista, P.J. Martel, C.M. Soares, Simulation of electron-proton coupling with a Monte Carlo method: application to cytochrome c3 using continuum electrostatics, *Biophys. J.* 76 (1999) 2978–2998.
- [98] A.M. Baptista, C.M. Soares, Some theoretical and computational aspects of the inclusion of proton isomerism in the protonation equilibrium of proteins, *J. Phys. Chem. B* 105 (2001) 293–309.
- [99] V.H. Teixeira, C.A. Cunha, M. Machuqueiro, A.S.F. Oliveira, B.L. Victor, C.M. Soares, A.M. Baptista, On the use of different dielectric constants for computing individual and pairwise terms in Poisson–Boltzmann studies of protein ionization equilibrium, *J. Phys. Chem. B* 109 (2005) 14,691–14,706.
- [100] C. Oostenbrink, A. Villa, A.E. Mark, W.F. van Gunsteren, A biomolecular force field based on the free enthalpy of hydration and solvation: the GROMOS force-field parameter sets 53A5 and 53A6, *J. Comput. Chem.* 25 (2004) 1656–1676.
- [101] M.J. Frisch, G.W. Trucks, H.B. Schlegel, G.E. Scuseria, M.A. Robb, J.R. Cheeseman, V.G. Zakrzewski, J.A. Montgomery, R.E. Stratmann, J.C. Burant, S. Dapprich, J.M. Millam, A.D. Daniels, K.N. Kudin, M.C. Strain, O. Farkas, J. Tomasi, V. Barone, M. Cossi, R. Cammi, B. Mennucci, C. Pomelli, C. Adamo, S. Clifford, J. Ochterski, G.A. Petersson, P.Y. Ayala, Q. Cui, K. Morokuma, D.K. Malick, A.D. Rabuck, K. Raghavachari, J.B. Foresman, J. Cioslowski, J.V. Ortiz, B.B. Stefanov, G. Liu, A. Liashenko, P. Piskorz, I. Komaromi, R. Gomperts, R.L. Martin, D.J. Fox, T. Keith, M.A. Al-Laham, C.Y. Peng, A. Nanayakkara, C. Gonzalez, M. Challacombe, P.M.W. Gill, B.G. Johnson, W. Chen, M.W. Wong, J.L. Andres, M. Head-Gordon, E.S. Replogle, J.A. Pople, Gaussian 98, Gaussian, Inc., Pittsburgh, PA, USA, 1998.
- [102] C.I. Bayly, P. Cieplak, W. Cornell, P.A. Kollman, A well-behaved electrostatic potential based method using charge restraints for deriving atomic charges: the RESP model, *J. Phys. Chem.* 97 (1993) 10,269–10,280.
- [103] B. Hess, C. Kutzner, D. van der Spoel, E. Lindahl, GROMACS 4: algorithms for highly efficient, load-balanced, and scalable molecular simulation, *J. Chem. Theory Comput.* 4 (2008) 435–447.
- [104] W.F. van Gunsteren, H.J.C. Berendsen, Computer simulation of molecular dynamics: methodology, applications, and perspectives in chemistry, *Angew. Chem. Int. Ed. Engl.* 29 (1990) 992–1023.
- [105] J.A. Barker, R.O. Watts, Monte Carlo studies of the dielectric properties of water-like models, *Mol. Phys.* 26 (1973) 789–792.
- [106] I.G. Tironi, R. Sperb, P.E. Smith, W.F. van Gunsteren, A generalized reaction field method for molecular dynamics simulations, *J. Chem. Phys.* 102 (1995) 5451–5459.
- [107] P.E. Smith, W.F. van Gunsteren, Consistent dielectric properties of the simple point charge and extended simple point charge water models at 277 and 300 K, *J. Chem. Phys.* 100 (1994) 3169–3174.
- [108] J. Hermans, H.J.C. Berendsen, W.F. Van Gunsteren, J.P.M. Postma, A consistent empirical potential for water–protein interactions, *Biopolymers* 23 (1984) 1513–1518.
- [109] W.F. van Gunsteren, H.J.C. Berendsen, Thermodynamic cycle integration by computer simulation as a tool for obtaining free energy differences in molecular chemistry, *J. Comput. Aided Mol. Des.* 1 (1987) 171–176.
- [110] D.L. Beveridge, F.M. DiCapua, Free energy via molecular simulation: applications to chemical and biomolecular systems, *Annu. Rev. Biophys. Biophys. Chem.* 18 (1989) 431–492.